In vitro degradation, photo-dynamic and thermal antibacterial activities of Cu-bearing chlorophyllin-induced Ca–P coating on magnesium alloy AZ31

Zhen-Yu Zhang [a], Yan-Lin An [a], Xiao-Shi Wang [a], Lan-Yue Cui [a,*], Shuo-Qi Li [a], Cheng-Bao Liu [a], Yu-Hong Zou [b], Fen Zhang [a], Rong-Chang Zeng [a,c]

[a] College of Materials Science and Engineering, Shandong University of Science and Technology, Qingdao, 266590, China
[b] College of Chemical and Biological Engineering, Shandong University of Science and Technology, Qingdao, 266590, China
[c] School of Materials Science and Engineering, Zhengzhou University, Zhengzhou, 450002, China

ARTICLE INFO

ABSTRACT

Surgical failures, caused by postoperative infections of bone implants, are commonly met, which cannot be treated precisely with intravenous antibiotics. Photothermal therapy (PTT) and photodynamic therapy (PDT) have attracted widespread attention due to their non-invasive antibacterial effects on tissues and no bacterial resistance, which may be an excellent approach to solve infections related to bone implants for biodegradable magnesium alloys. Herein, a sodium copper chlorophyllin (SCC) with a porphyrin ring induced Ca–P coating was prepared on AZ31 magnesium alloy via layer-by-layer (LbL) assembly. The morphology and composition of the samples were characterized through field emission scanning electron microscope (FE-SEM) with affiliated energy dispersive spectrometer (EDS), X-ray diffractometer (XRD), and Fourier infrared spectrometer (FTIR) and X-ray photoelectron spectrometer (XPS) as well. Potentiodynamic polarization, electrochemical impedance spectroscopy (EIS) and hydrogen evolution experiments were employed to evaluate the corrosion behavior of the samples. Atomic absorption spectrophotometer was used to measure Cu elemental content of different immersion periods. Cytocompatibility and antibacterial performance of the coatings were probed using *in vitro* cytotoxicity tests (MTT assay), live/dead cell staining and plate counting method. The results showed that the obtained $(Ca–P/SCC)_{10}$ coating exhibited good corrosion resistance, antimicrobial activity (especially under 808 nm irradiation) and biocompatibility. The antibacterial rates for *E. coli* and *S. aureus* were 99.9% and 99.8%, respectively; and the photothermal conversion efficiency was as high as 42.1%. Triple antibacterial mechanisms including photodynamic, photothermal reactions and copper-ions release were proposed. This coating exhibited a promising application for biodegradable magnesium alloys.

1. Introduction

Magnesium (Mg) and its alloys have the advantages of biodegradability, an elastic module close to the natural bone and appropriate mechanical properties. Their degradation product Mg^{2+} ions are also necessary for the growth of human tissues; and herein they can be used as internal fixation material to avoid secondary operations [1–3]. However, the rapid degradation rate restricts the orthopedic application of Mg alloys.

Generally, Ca–P coating, with excellent biocompatibility and osseointegration, can be used to mitigate the degradation rate of Mg alloys [4,5]. In recently years, many methods have been reported for the preparation of Ca–P coatings on Mg alloys. For example, Surmeneva et al. [6,7] obtained a uniform and pore-free HA coating on AZ91 magnesium alloy via RF magnetron sputter deposition followed by post-deposition annealing, which had superior bonding strength and enhanced chemical reactivity. Han et al. [8] used the dropwise addition procedure during the electro-deposition process to prepare Ca–P coating on pure Mg plates. The main components of the Ca–P coating were hydroxyapatite (HA) and calcium hydrogen phosphate dihydrate, which exhibited excellent corrosion resistance in simulated body fluids. In our previous work, DNA was used to induce Ca–P coating on AZ31 by means of hydrothermal method [9], led to an improved corrosion resistance and adhesion strength compared with the Ca–P coating without DNA.
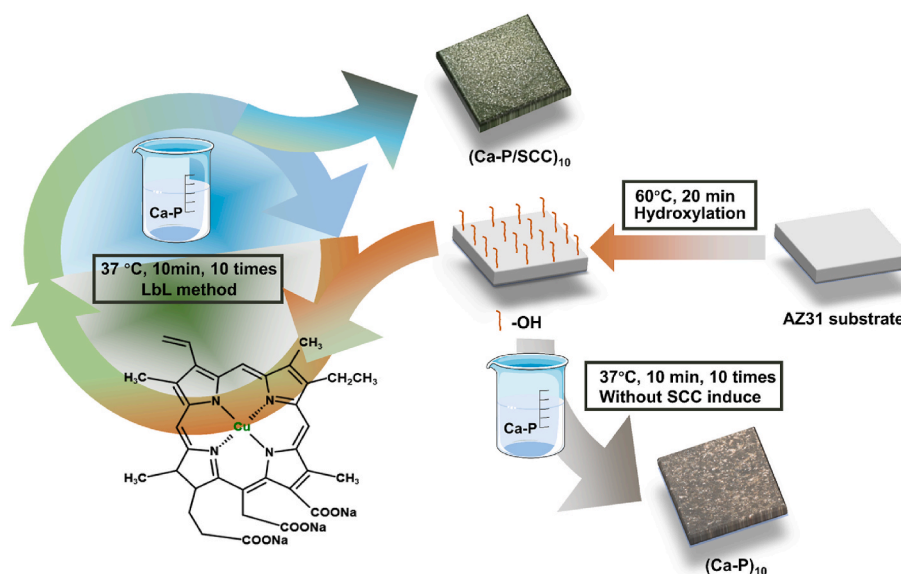
Fig. 1. Schematic diagram of (Ca–P/SCC)$_{10}$ and (Ca–P)$_{10}$ coatings fabricated via LbL method.

However, due to the limitations of temperature, voltage, pressure and other experimental conditions involved in the above preparation of the Ca–P coating, many macromolecules are difficult to be loaded into the coating, which limits the functionalization of the coating. Compared with the above mentioned methods, the prepared coating under mild experimental condition via layer-by-layer (LbL) assembling has advantages such as controllability, functionalization and molecular recognition for its good adhesion and homogeneity [10].

Obviously, the frequent postoperative infection of bone implants becomes one of the most serious complications, leading to implant failure and bacteria-infected organs [11]. At present, the methods to improve the antibacterial performance of biodegradable Mg alloys mainly include the addition of antibiotics [12,13], polypeptides [14], and co-doping with metal ions (substances that can release metal ions) [15–18]. Nevertheless, the antimicrobial resistance after using of antibiotics may limit its applications *in vivo* [19,20]. And the antibacterial activity of polypeptides is also limited.

Recently, photodynamic therapy (PDT) and photothermal therapy (PTT) have been employed to treat bacterial infections and cancers under photo irradiation, which attract more and more attentions due to their wide antibacterial spectrum, no microbial resistance and fast bacteriostasis response [21–23]. Photosensitizers (PSs) is a key link in PDT process to generate reactive oxygen species (ROS) [24], especially for singlet oxygen ($^1O_2$), which can cause a damage in cellular membranes and subsequently kills tumor cells or bacteria [25]. Unfortunately, both PS-mediated oxygen consumption and blood vessel damage further potentiate tissues hypoxia. The scenario hinders the effect of PDT treatment [26,27]. Oxygen-independent therapies (i.e., PTT) are an effective solution to hypoxia [28]. Upon selective photo treatment, PTT agents absorb light and dissipate the absorbed energy through non-radiative decay (heating), leading to an increase in the temperature of the local environment [29,30], which can promote blood circulation and oxygen transportation around the tissues. But if the temperature is too high, it will cause irreversible damage of healthy cells. Thus, there is an acceptable temperature in human body for PTT. Note that, some bacteria can survive at a temperature of 70 °C. The highest temperature that human tissues, however, can tolerate is between 50 and 60 °C, which leads to a significant reduction in the antibacterial efficiency of PTT in the body [31]. Duan et al. [32] designed a cascade synergistic immunotherapy nano-system, in which polydopamine was used as a photothermal agent to induce low-temperature PTT, leading to immunogenic cell death, activating dendritic cells, and enhancing the antitumor

immune response of T cells.

Thus, it is necessary to combine PDT and PTT to achieve a good antibacterial ability. Li et al. [33] used hybrid nanosheets of g–C$_3$N$_4$–Zn^{2+}@graphene oxide (SCN–Zn^{2+}@GO) to expose in the light with a wavelength of 660 and 808 nm for a short time; under the synergistic effect of PDT and PTT antibacterial treatment, the antibacterial ratio was greater than 99.1%. The wound healing of Zn^{2+} ions was evaluated, but the antibacterial effects influenced by the release of Zn^{2+} ions was ignored. Note that, the application of PTT and PDT on nanomaterials can quickly eliminate infection, promote wound healing or anti-tumor effect, but the combined applications of PTT and PDT on metallic alloys have been rarely reported.

Porphyrins have been noted to have a special molecular structure, and may be a promising PS candidate for the active layer on bio-metallic materials due to the highly photosensitive properties, strong two-photon absorption, and efficient electron transfer as well as excellent thermal stability. This scenario is attributed to the natural structure and photoharvesting with a large π-conjugation on the carbon-nitrogen macrocyclic framework [34–38]. And they can produce ROS [39] and heat [40] under the light irradiation, involving intersystem crossing to triplet excited state, followed by the formation of singlet oxygen ($^1O_2$) [41], which is a highly reactive species and mediates various oxidative processes.

Sodium copper chlorophyllin (SCC) is a water-soluble sodium salt of copper extracted from chlorophyll with good biocompatibility, which has been used as food dye and wound healing promoter for decades [42]. And in recent years, the anti-cancer activity of SCC has been paid close attention in the field of nano biomaterials based on its good effect in PDT or PTT therapy. Both Chu et al. [43] and Pemmaraju et al. [44] reported that chlorophyll molecules, obtained from plants, were encapsulated into polymer composite nanomaterials for cancer imaging and targeted cancer therapy, exhibiting excellent PTT or PDT properties with low cytotoxicity.

On the other hand, the role of the Cu^{2+} ion in the center of the SCC structure cannot be underestimated. The Cu^{2+} ion is an indispensable micronutrient element for human health, which plays an important role in human enzymes and promotes the production of cell respiration, neurotransmitters and peptide hormones. Cu^{2+} ions also have good antibacterial properties through trigger decomposition of S-nitrosothiols (RSNOs) in the body and generate NO [45], which reacts with free radical superoxide to form reactive byproducts (peroxynitrite and dinitrogen trioxide), causing the membrane disruption and cell

dysfunction of bacteria [46,47], like *influenza A* virus, *Staphylococcus aureus* (*S. aureus*), and *Escherichia coli* (*E. coli*) together with *Listeria monocytogenes* [48,49], thereby promoting the regulation of bacteria in the tissues near the bone implant. In addition, Cu^{2+} ions can regulate the action of a variety of cytokines and the growth factors and stimulate angiogenesis and collagen deposition, promoting wound healing effectively [50,51]. Thus, SCC may provide triple antibacterial activity, including PDT, PTT and Cu^{2+} ions release after the demetalation reaction.

In this study, 10 bilayers of Ca–P coatings were induced by SCC on the surface of the AZ31 alloy using the LbL method. The purpose aims to take deep insight into the coating formation and corrosion and antibacterial mechanisms by fabricating a Cu bearing $(Ca–P/SCC)_{10}$ coating with superior corrosion resistance, PTT and PDT antibacterial performance together with good biocompatibility.

2. Experimental

2.1. Materials and reagents

AZ31 substrate (Al 2.5–3.0 wt%, Zn 0.7–1.3 wt%, Mn > 0.2 wt% and the balanced Mg) sheets were bought from Shandong Yinguang Yuyuan Light Metal Precise Forming Co., Ltd., China. Sodium copper chlorophyllin (SCC), beef powder and peptone used in the culture medium in the antibacterial experiment were purchased by Xiya Reagent Co., Ltd., China. $Ca(NO_3)_2 \cdot 4H_2O$ and $NaH_2PO_4 \cdot 2H_2O$ was obtained by Tianjin Guangfu Technology Development Co., Ltd. The AZ31 sheets were cut into squares with a size of 20 mm × 20 mm × 5 mm, ground smoothly with 2500 grit SiC sandpaper, then rinsed with alcohol and deionized water, and finally dried with warm air.

2.2. Composite coating preparation

The preparation process of $(Ca–P/SCC)_{10}$ coatings is shown in Fig. 1. Firstly, AZ31 substrate was immersed in 1 M NaOH solution at 60 °C for 20 min for hydroxylation. Then, the hydroxylated samples were alternately dipped in the SCC solution (0.01 g/L SCC) and calcium-phosphorus (Ca–P) solution (0.15 M $Ca(NO_3)_2 \cdot 4H_2O$ and 0.1 M $NaH_2PO_4 \cdot 2H_2O$) with tender stir for 10 min at 37 °C. After 10 cycles, the obtained coating was designated as $(Ca–P/SCC)_{10}$ coating, which was dried in oven at 70 °C for 1 h. The $(Ca–P)_{10}$ coating as a control was directly immersed in a Ca–P solution on a hydroxylated AZ31 substrate for 10 times.

2.3. Surface characterization

Field emission scanning electron microscopy (FE-SEM, Nova Nano SEM 450, FEI, USA) was used to observe the microscopic and cross-sectional morphologies of the samples. The energy dispersive X-ray spectroscope (EDS), attached to the FE-SEM instrument, was utilized for analysis the surface elements of coatings at an acceleration voltage of 15 kV. X-ray diffractometer (XRD, Rigaku D/MAX 2500 PC, Japan) was employed to detect the phase composition with a Cu target at a scanning rate of 0.02 s^{-1} in the 2θ range of 10°–90°. Fourier infrared spectrometer (FTIR, Nicolet 380, Thermo Electron Corporation, USA) was conducted to characterize the main functional groups of the sample surface between $400–4000 \text{ nm}^{-1}$. X-ray photoelectron spectrometer (XPS, Nexsa, Thermo Fisher Scientific Inc., USA) was employed to characterize the bonding modes of the coatings using Al Kα radiation (1486.6 eV), binding energies were measured with a precision of ±0.1. Atomic absorption spectrophotometer (PERSEE TAS-986F, China) was used to measure the Cu element content released from the coatings in triplicate with different immersion times.

2.4. Corrosion testing

The corrosion resistance of the $(Ca–P/SCC)_{10}$ coating was characterized by electrochemical experiments. Hank's balanced salt solution (HBSS) was selected as the corrosive medium. Potentiodynamic polarization curves and electrochemical impedance spectroscopy (EIS) were conducted on an electrochemical workstation (PAR Model 2273, Princeton Applied Research, USA) with a three-electrode system. The sample was the work electrode; saturated calomel electrode (SCE) and a platinum plate acted as the reference and counter electrodes, respectively. Polarization resistance (R_p) was calculated using Stern-Geary equation [52]:

$$R_p = \frac{\beta_a \cdot \beta_c}{2.303 i_{corr}(\beta_a + \beta_c)} \tag{1}$$

where, β_a and β_c are Tafel slopes of anodic and cathodic polarization curves, respectively; and i_{corr} represents the corrosion current density of the samples. The hydrogen evolution and immersion tests were used to monitor the corrosion resistance of the AZ31 substrate and coatings during the degradation process. The specific experimental plan is displayed in the supporting information.

2.5. Antimicrobial test

In order to evaluate the PTT and PDT abilities of the samples, gram-positive *S. aureus* and gram-negative *E. coli* were selected to co-culture with the samples for testing. Place the UV-sterilized samples and 5 mL of bacteria solution in a six-well plate, and put them in the dark, white light (1 W cm^{-2}) and 808 nm near-infrared (NIR) light (1 W cm^{-2}) conditions. After 30 min of co-cultivation, the mixture was serially diluted for 1000-fold and 100 μL of each suspension with 0.85 wt% NaCl was evenly plated onto the culture medium in triplicate. Finally, the culture medium was incubated in an incubator at 37 °C for 24 h to count the number of bacterial colonies. The composition of the culture medium and the method of culturing the bacterial cells are shown in the supporting information.

2.6. ROS release and photothermal performance tests

ROS fluorescent probe 2,7-dichlorodihydrofluorescein diacetate (DCFH-DA) were used to evaluate the PDT ability of the samples within 15 min under irradiation of P1 adjustable integrated semiconductor laser light source (P1, Hi-Tech Optoelectronics Co., Ltd, China, 0.5 W/cm^2). DCFH-DA does not show fluorescence, but it can be rapidly oxidized to a highly fluorescent molecule (2′,7′-dichlorofluorescein) in the presence of ROS [53]. The fluorescence intensity was measured using a ROS assay kit (Cat#S0033, Beyotime Biotechnology Co., Ltd, China). For the photothermal tests, the samples were irradiated by the P1 light source with an intensity of 1 W/cm^2; and the temperature change was recorded with an infrared thermal imager (PTi120, Fluke testing instrument Shanghai Co., Ltd, China).

In order to intuitively express the ability for $(Ca–P/SCC)_{10}$ coating to convert light to heat, the photothermal conversion efficiency (η) was calculated according to the literature [54]. The energy balance of the whole system is shown below:

$$\sum_i m_i c_{p,i} \frac{dT}{dt} = Q_{SCC} + Q_s + Q_{loss} \tag{2}$$

where, c and m represent the mass and heat capacity, respectively; the suffix "i" of c and m refers to the solvent (water) or dispersed matter (nanoparticles) [24]. T is the solution temperature. Q_{SCC} and Q_s represent the photothermal energy absorbed by $(Ca–P/SCC)_{10}$ coating and the heat associated with the light absorbed by solvent per second, respectively. Q_{loss} is the heat released by the system into the environment.
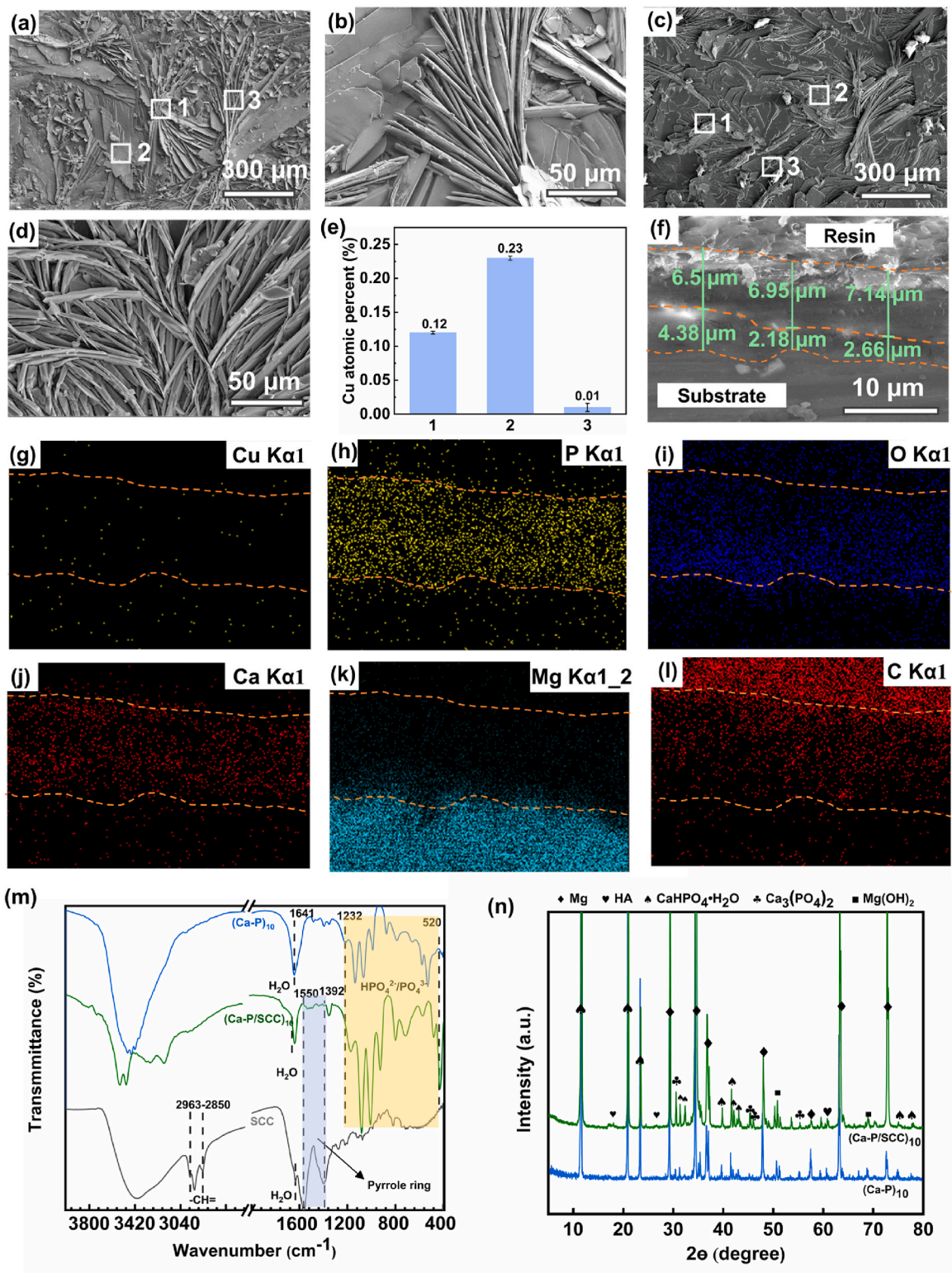
Thereinto,

Fig. 2. SEM images of (a and b) (Ca–P/SCC)$_{10}$ and (c and d) (Ca–P)$_{10}$ coatings and corresponding EDS spectra of Cu element for the (Ca–P/SCC)$_{10}$ coating; (f) Cross-sectional image and corresponding (g–l) EDS mapping images of the (Ca–P/SCC)$_{10}$ coating; (m) FTIR spectra of pure SCC, (Ca–P/SCC)$_{10}$ and (Ca–P)$_{10}$ coatings; (n) XRD pattern of the (Ca–P)$_{10}$ and (Ca–P/SCC)$_{10}$ coatings.

$$Q_{SCC} = I\left(1 - 10^{-A_\lambda}\right)\eta \tag{3}$$

$$Q_{loss} = hA\Delta T \tag{4}$$

In heating pure water, the heat input is equal to the heat output at the maximum steady-statue temperature:

$$Q_s = Q_{loss} = hA\Delta T_{max,\ H_2O} \tag{5}$$

where, h and A are the heat transfer coefficient and the surface area of the container, respectively. ΔT is the change in temperature, which is referred to T-T_{surr} (T and T_{surr} are the solution temperature and ambient
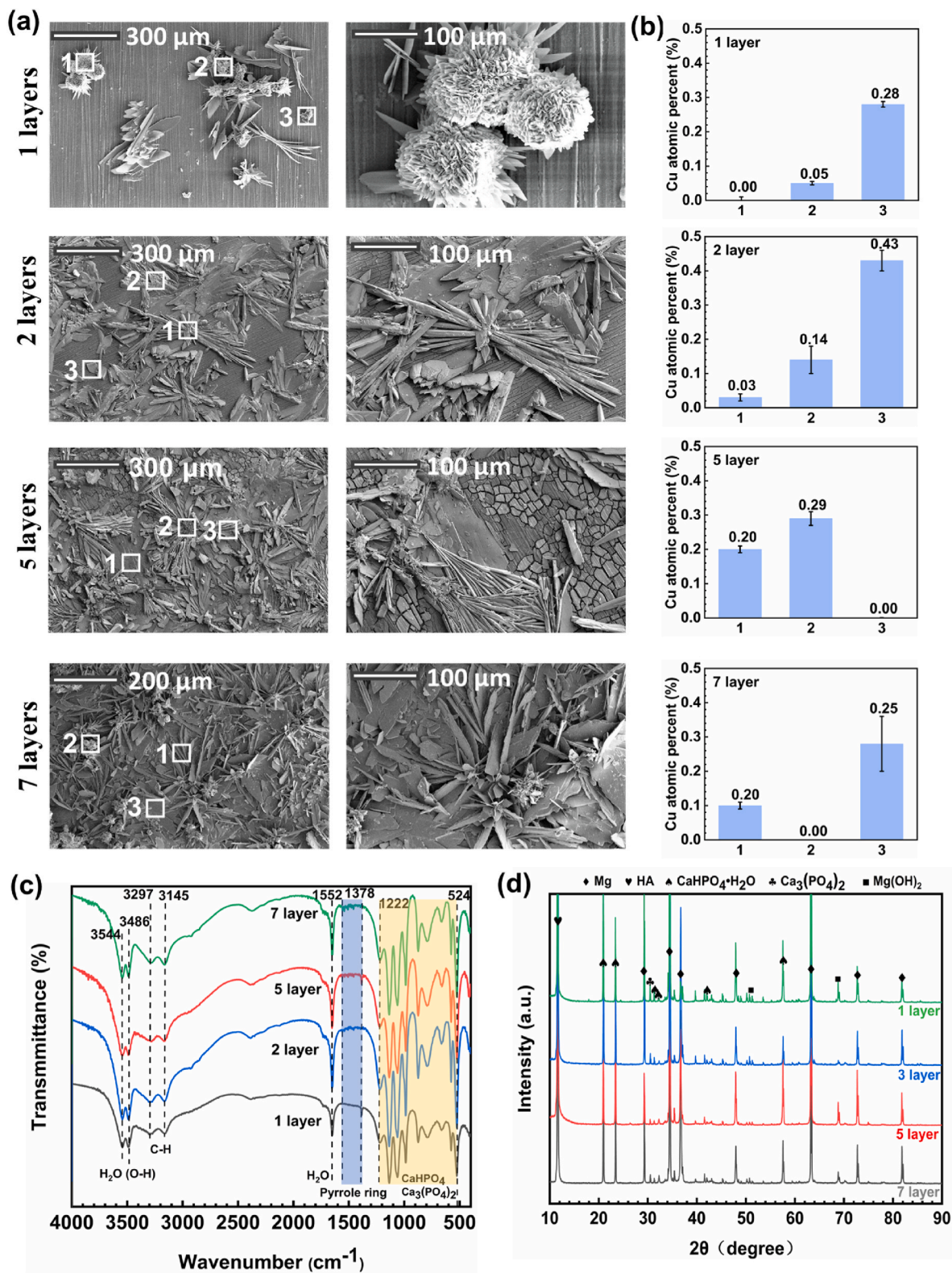
Fig. 3. (a) SEM images, corresponding (b) EDS analysis of Cu element, (c) FTIR spectra and XRD patterns of the (Ca–P/SCC)₁₀ coating with 1, 2, 5 and 7 bilayers.

temperature of the surrounding, respectively). $\Delta T_{max,\,H_2O}$ is the temperature change in the equilibrium state of the water in the system.

For the photothermal experiment of the (Ca–P/SCC)₁₀ coating, the heat absorption in the system is the sum of the heat generated by the sample (Q_{SCC}) and the heat generated by water (Q_s), equal to the heat output at the maximum steady state-temperature, so the equation can be reduced to:

$$Q_s + Q_{SCC} = Q_{loss} = hA\Delta T_{max,\,mix} \tag{6}$$

$\Delta T_{max,\,mix}$ is the temperature change of the (Ca–P/SCC)₁₀ coating at the maximum steady state, the photothermal conversion efficiency formula can be obtained from formulas (2), (4) and (5):
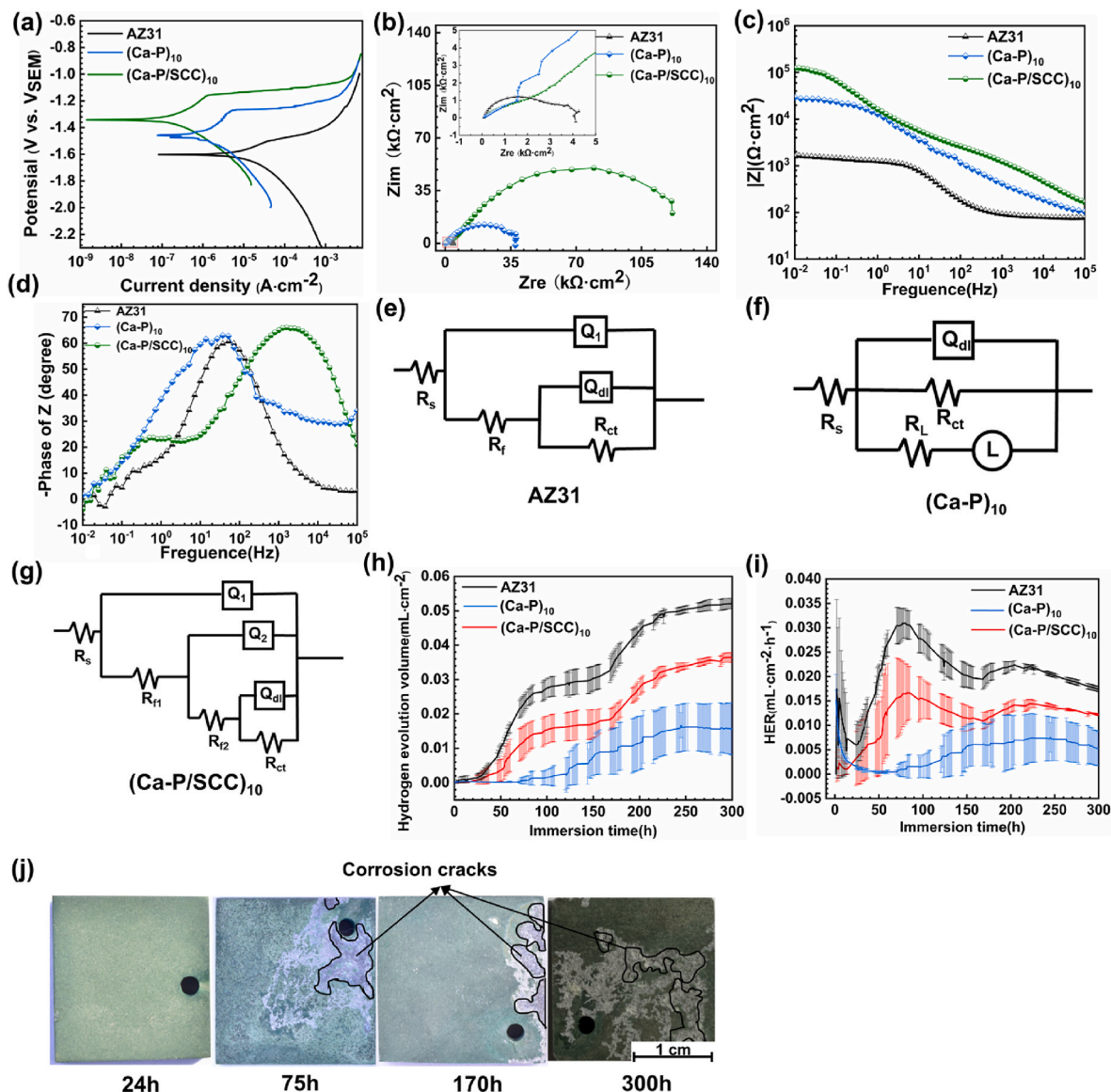
Fig. 4. (a) Potentiodynamic polarization, (b) Nyquist plots and (c, d) Bode plots of the AZ31 substrate, (Ca–P)$_{10}$ and (Ca–P/SCC)$_{10}$ coatings; corresponding EC model of the (e) AZ31 substrate, (f) (Ca–P)$_{10}$ and (g) (Ca–P/SCC)$_{10}$ coating; the (h) HEV and (i) HER curves of AZ31 substrate, (Ca–P)$_{10}$ and (Ca–P/SCC)$_{10}$ coatings and corresponding (j) macroscopic morphology of the (Ca–P/SCC)$_{10}$ coatings after an immersion of 24, 75, 170 and 300 h.

$$\eta = \frac{hA\left(\Delta T_{max,mix} - \Delta T_{max, H_2O}\right)}{I\left(1 - 10^{-A_\lambda}\right)} \quad (7)$$

In order to calculate hA, θ is introduced and defined as the ratio of ΔT and ΔT_{max}:

$$\theta = \frac{\Delta T}{\Delta T_{max}} \quad (8)$$

When the laser is off, $Q_{SCC} + Q_s = 0$.
Thus,

$$t = -\frac{\sum_i m_i C_{p,i}}{hA} \ln\theta \quad (9)$$

Finally, the value of photothermal conversion efficiency (η) can be obtained by equation (6).

2.7. Cytotoxicity test

Mouse MC3T3-E1 pre-osteoblasts were used as experimental targets to evaluate the cytotoxicity of the (Ca–P/SCC)$_{10}$ coating. The specific

operation steps and detection methods of this experiment are shown in the supporting information [55].

In order to get a credible conclusion, t-test was employed as statistical analysis for biocompatibility measurements. All data were shown in the form of means $\pm$ standard deviations ($n = 3$, mean $\pm$ SD, p* < 0.05, p** < 0.01, p*** < 0.001, p**** < 0.0001). When $p < 0.05$, it was regarded as statistically significant.

3. Results

3.1. Surface analysis

SEM images of (Ca–P/SCC)$_{10}$ and (Ca–P)$_{10}$ coatings are shown in Figure 2a–d. A dense (Ca–P/SCC)$_{10}$ coating with lamellar-like structures is formed on the AZ31 alloy, and the length of the leafs reaches to 250–300 μm; while the stalk-like (Ca–P)$_{10}$ coating alternately grows along the direction of the magnet stirring, the stalk-like structure reaches a length of 350–400 μm. The corresponding EDS data is displayed in Fig. S1 and Fig. 2e. The main components of the (Ca–P/SCC)$_{10}$ coating

with a Ca/P ratio of 1.12 ± 0.9 are C, O, P and Ca elements (Figure S1a), the missing Mg element can be ascribed to the complete coverage of the lamellar-like coating. The presence of Cu elements confirms the loading of SCC (Fig. 2e). The different Cu elemental content among point 1–3 can be inferred that SCC absorbed on the laminae of the $(Ca–P/SCC)_{10}$ coating can be acted as the nucleation center to induce the coating formation. The components of the $(Ca–P)_{10}$ coating also are C, O, P and Ca elements (Figure S1b) and the Ca/P ratio (0.92 ± 0.06) is slightly lower than that of $(Ca–P/SCC)_{10}$ coating.

The cross-sectional morphology and elemental distribution of $(Ca–P/SCC)_{10}$ coating is shown in Fig. 2f-l. The coating can be roughly divided into two layers: the thickness of outer layer with high Ca and P elements is about $6.86 \mu m \pm 0.33$; the preferentially formed Mg- and Ca–P conversion layer close to the substrate with a higher content of Mg, O and P elements, has a thickness of approximately $3.07 \mu m \pm 1.16$. It is too difficult to judge the distribution of SCC molecules (Fig. 2g) in the composite coating, due to its less adsorbed amount. However, they can be confirmed by the next FTIR and XPS analysis (Figure 2m and 6).

XRD patterns and FTIR spectra are collected to identify the composition of $(Ca–P/SCC)_{10}$ and $(Ca–P)_{10}$ coatings, as shown in Fig. 2m and n. In the FTIR spectra, pure SCC powder was used as the control, the vibration of -ONa exists at the peak of 3400 cm^{-1}. The peaks for stretching vibration of unsaturated –CH = bond is displayed around 2963-2850 cm^{-1}, generating a bathochromic shift due to the conjugation effect of the SCC molecules [56]. The C=C stretching vibration and –CH$_3$ bending vibration appear at 1550 and 1392 cm^{-1}, respectively. And the peaks near 1064 cm^{-1} and around 1064-1550 cm^{-1} represent the C–N bond and the skeleton of the porphyrin ring [56–59]. For the $(Ca–P/SCC)_{10}$ coating, the porphyrin ring vibration is found at 1392-1550 cm^{-1}, which proves that SCC is loaded sucessfully. And peaks at 520-1120 cm^{-1} demonstrate the formation of Ca–P products containing HPO$_4^{2-}$ and PO$_4^{3-}$, agreeing with the results of above-mentioned SEM and EDS. The XRD patterns (Figure 2n) further confirm that the main compositions of the two Ca–P coatings are CaHPO$_4$·H$_2$O, HA, Ca$_3$(PO$_4$)$_2$ and Mg(OH)$_2$. The presence of Mg(OH)$_2$ reflets that the Mg substrate degrades during the coating formation process. CaHPO$_4$·H$_2$O formed at the initial formation of the coatings, verifying the results obtained from Fig. 2f-l. No peaks related to magnesium phosphate are found in the XRD pattern, due to the trace content and the cover of the outer $(Ca–P/SCC)_{10}$ coating.

3.2. Film formation process

In order to explore the nucleation and growth process of $(Ca–P/SCC)_{10}$ coating, 1, 2, 5 and 7 bilayers were selected to represent different stages of coating formation, in which 1 and 2 bilayers are the initial stage, and 5 and 7 bilayers are the intermediate stage. SEM images with different number of bilayers and the corresponding EDS data are shown in Fig. 3a, b and S2. After an assembly of 1 bilayer, SCC absorbs on the surface of AZ31 substrate, and some clusters of Ca–P structures with radial leaves appear. For 2 bilayers, the surface of the substrate begins to chap under the effect of immersion, and laminar Ca–P product grows to cover part of the substrate. When the coating reaches to 5 bilayers, the dry river bed-like corrosion cracks expand, and the Ca–P coating covers most of the substrate surface. The Ca–P lamina nucleates and grows in the sites of new deposited SCC in further. When the number of the bilayer comes to 7, the substrate is completely covered by Ca–P products, and the coating becomes denser. Thus, the adsorption of SCC acts as a center of nucleation and growth for the clusters of Ca–P products. EDS spectra reveal that the main composition of the Ca–P coating was C, O, P, Ca (Fig. S2) and a spot of Cu (Fig. 3b), which is not varied with the changes of the bilayer number, confirming the homogeneity of each bilayer for the $(Ca–P/SCC)_{10}$ coating. Note that, the Ca/P ratio around the nucleation center is higher than the other site of the Ca–P lamina, and SCC tends to absorb on the flat part of the Ca–P lamina to initiate the formation of the new Ca–P products.

FTIR spectra and XRD patterns of the $(Ca–P/SCC)_{10}$ coating during film formation process is exhibited in Fig. 3c and d. The vibration peaks of the porphyrin ring skeleton are found at 1378-1552 cm^{-1} with very weak intensity due to the low content of SCC. The characteristic peaks of HPO$_4^{2-}$ and PO$_4^{3-}$ appear between 524 and 1222 cm^{-1}, which are confirmed as Ca$_3$(PO$_4$)$_2$, CaHPO$_4$ and HA by the XRD patterns. During the induction process, there are no obvious changes in chemical compositions of the coatings, agreeing with the results of above EDS spectra.

3.3. Corrosion behaviors

Potentiodynamic polarization curves and corresponding data of the AZ31 substrate, $(Ca–P)_{10}$ and $(Ca–P/SCC)_{10}$ coatings in Hank's solution are shown in Fig. 4a, Tables S1 and S2. As shown in Table S1, the corrosion current density (i_{corr}) of $(Ca–P/SCC)_{10}$ coating (1.35×10^{-7} A cm^{-2}) is smaller than AZ31 substrate (5.45×10^{-6} A cm^{-2}) and $(Ca–P)_{10}$ coating (7.23×10^{-6} A cm^{-2}), which provides a good corrosion protection. And the corrosion potential (E_{corr}) of the $(Ca–P/SCC)_{10}$ coating increases 0.27 V/SCE in the positive direction compared with the bare AZ31 alloy, implying an increase in the tendency of corrosion initiation from a thermodynamics perspective. Both two coatings show a significant breakdown potential, proving the dissolution in anode zone is suppressed due to the formation of a passivation film. Moreover, the increased anodic Tafel slope (β_a) and decreased cathodic Tafel slope (β_c) also reflect a more positive modification of the $(Ca–P/SCC)_{10}$ coatings, agreeing with the R_p values of the samples.

Nyquist and Bode plot of the AZ31 substrate, $(Ca–P)_{10}$ and $(Ca–P/SCC)_{10}$ coatings are displayed in Fig. 4b–d. The diameters of the capacitive reactance arcs for $(Ca–P/SCC)_{10}$ coating is much larger than the AZ31 substrate and $(Ca–P)_{10}$ coating, confirming the $(Ca–P/SCC)_{10}$ coating has the best protection from corrosion. In the Bode plot (Fig. 4c and d), the low-frequency platform of $(Ca–P/SCC)_{10}$ coating with three different time constants is one order of magnitude higher than the $(Ca–P)_{10}$ coating, and two orders of magnitude higher than the AZ31 substrate, agreeing with the results of the Nyquist plot.

Consequently, three kinds of equivalent circuits (EC) models can be used to fit the EIS plots as shown in Fig. 4e–g, and the electrochemical data of EC model is displayed in Table S2. The EC model of AZ31 substrate shows two obvious time constants in Fig. 4e, which can be described as $R_s(Q_1(R_f(Q_{dl}R_{ct})))$, where Q_l and R_f are the double layer capacitance and resistance of corrosion product film, and R_{ct} and R_s represent the degree of impedance against the corrosion and the solution resistance between the electrode and the samples [60]. As shown in Fig. 4f. The EC model of $(Ca–P)_{10}$ coating presents a high frequency capacitor loop composed of Q_{dl} and R_{ct}, implying double layer capacitance and charge transfer resistance of the $(Ca–P)_{10}$ coating. The inductance L and resistance R_L in the low frequency region symbolize the pitting of the exposed substrate or peeling of the coating [61,62], which can be confirmed by the above loose structure in *3.1*. For the $(Ca–P/SCC)_{10}$ coating in Fig. 4g, the electric double layer is composed of a constant phase component (Q_{dl}) and a charge transfer resistance (R_{ct}) in series, represents the high-frequency circuit, and related to the electric double layer between the electrolyte and the working electrode [63, 64]. The loop of the intermediate frequency range is related to the corrosion process of the $(Ca–P/SCC)_{10}$ coating, which is represented by R_{f2}, Q_2. The low frequency capacitive loop is related to resistance of Mg(OH)$_2$ corrosion product film, which can be represented by resistors R_{f1} and Q_1 in series. The missing pitting phenomenon and increased time constant of $(Ca–P/SCC)_{10}$ coating indicate that $(Ca–P/SCC)_{10}$ coating has better corrosion resistance than the other two samples [62,65,66].

The hydrogen evolution volume (HEV) and hydrogen evolution rate (HER) curves of the samples soaked in HBSS for 300 h is shown in Fig. 4h and i. The whole HEV of the $(Ca–P/SCC)_{10}$ coating was lower than that of the AZ31 substrate and higher than the $(Ca–P)_{10}$ coating. From the HER curves, for the AZ31 substrate, the Mg(OH)$_2$ corrosion products cause a decrease in the HER in the initial stage of immersion. After an
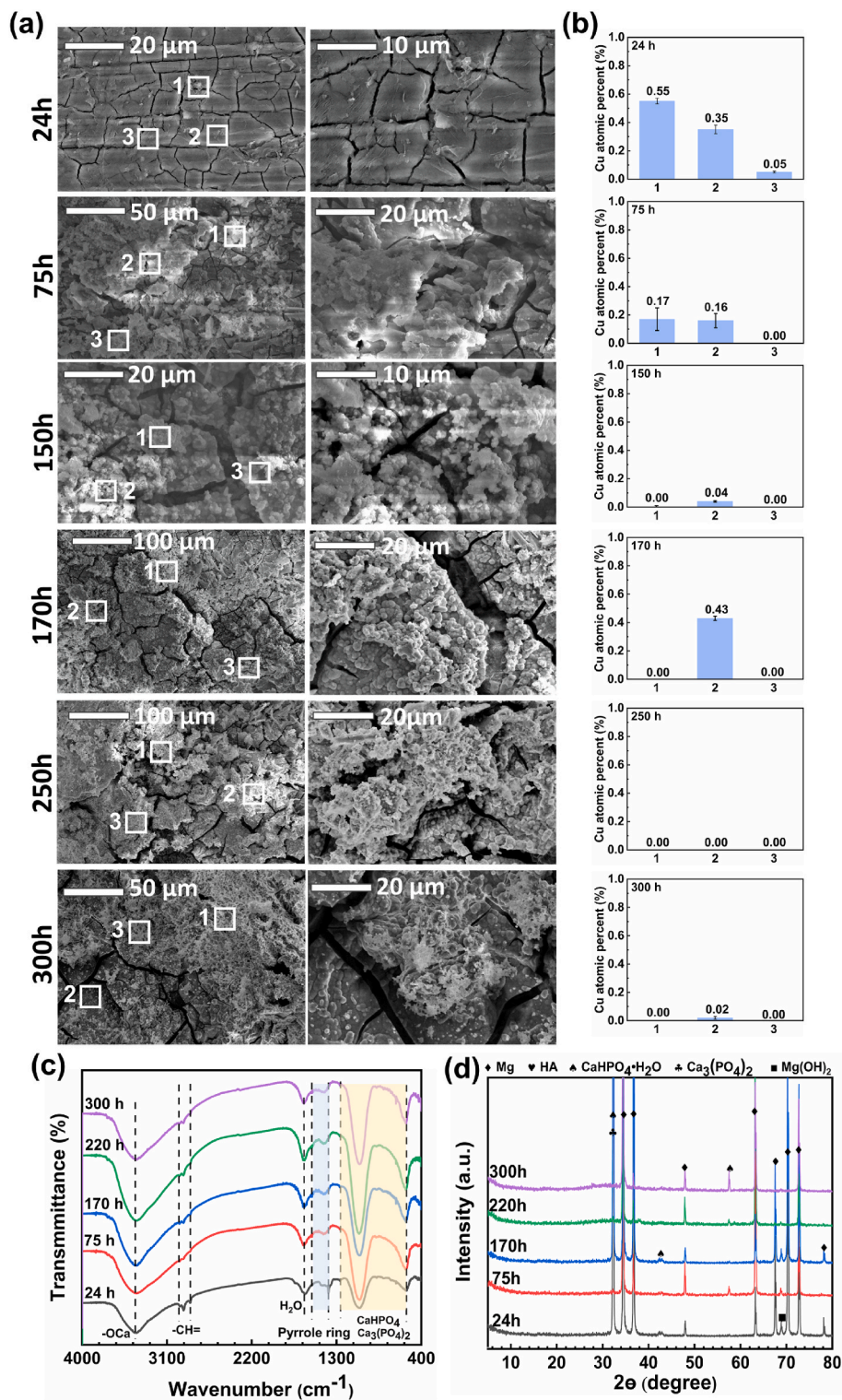
Fig. 5. (a) SEM images and corresponding (b) EDS spectra of Cu element for $(Ca–P/SCC)_{10}$ coating with an immersion of 24, 75, 150, 170, 250 and 300 h; (c) FTIR spectra and (d) XRD patterns of the sample after an immersion of 24, 75, 170, 220 and 300 h in HBSS.

immersion of 25 h, the corrosion product layer disables and the HER increases rapidly. With an immersion of 75 h, the depositions of Ca^{2+}, HPO_4^{2-} and PO_4^{3-} ions on the surface of the substrate form a new protective film, resulting in a lower HER. For the $(Ca–P)_{10}$ coating, HER declines rapidly within 50 h due to the physical barrier effect of the stalk Ca–P structure. During the 50–200 h period, the Ca–P structure degrades, and HER slowly rises. From immersing for 200–300 h, the

degradation of the coating and the formation of corrosion products gradually reach an equilibrium. For the $(Ca–P/SCC)_{10}$ coating, the decrease in HER in the early stage contributes to the physical barrier of the lamellar-like Ca–P coating. After a 10-h immersion, the large lamina of the coating might fall off, resulting an increase in HER. Then, corrosion products formed during the continued immersion occupy the surface of sample, resulting in a brief drop in HER. From 10 to 75 h of the
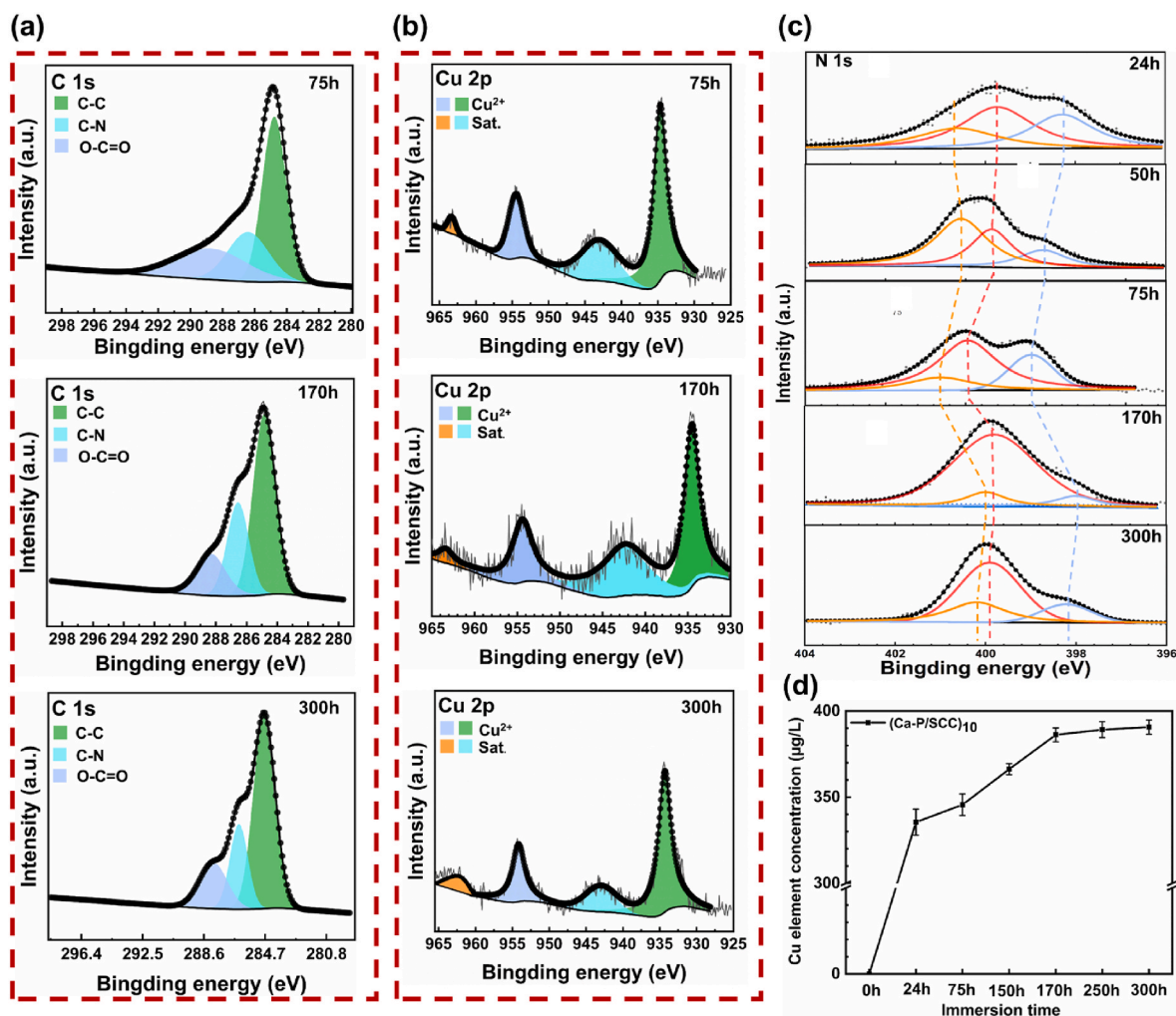
Fig. 6. (a, b, c) XPS spectra of C 1s, Cu 2p and N 1s for the (Ca–P/SCC)$_{10}$ coating with different immersion times. (d) Flame atomic absorption spectroscopy of the Cu elements released from the (Ca–P/SCC)$_{10}$ coating as function as immersion time.

immersion, obvious corrosion defects appear on the surface of the sample, due to the degradation of the Ca–P coating and the exposure of the AZ31 substrate. The scenario gradually leads to enhanced galvanic corrosion between the (Ca–P/SCC)$_{10}$ coating and the substrate or between the Al–Mn and α-Mg phase (Fig. 4j). Note that, the slope of the HER curve of the (Ca–P/SCC)$_{10}$ coating is bigger than AZ31 substrate at about 55–60 h, which might be due to a lot of released Cu^{2+} ions from porphyrin demetalation reaction participate in the galvanic corrosion, accelerating the HER. At about 200 h, the formation of corrosion products and corrosion of the samples reach a relative equilibrium. Although, in the early stage of immersion (before 20 h), the HER of the (Ca–P)$_{10}$ coating was higher than that of the (Ca–P/SCC)$_{10}$ coating, the general HER of the (Ca–P)$_{10}$ coating was lower than that of the (Ca–P/SCC)$_{10}$ coating, which also may be attributed to the galvanic corrosion caused by the SCC demetallization reaction.

Changes in morphology and composition of the (Ca–P/SCC)$_{10}$ coating after an immersion of 24, 75, 150, 170, 250 and 300 h are exhibited in Fig. 5 and Fig. S3. During 24 h, the lamellar-like (Ca–P/SCC)$_{10}$ coatings completely peel off and many corrosion cracks appear. The highest Cu content (Fig. 5b) has shed the (Ca–P/SCC)$_{10}$ coating, enhancing the galvanic corrosion or leading to the exposure of the inner SCC as the corrosion nucleation center, which would be confirmed by the next XPS spectra. After an immersion of 75 h, granular corrosion products begin to be formed. An immersion of 150 h later, new Ca–P precipitates are deposited on the surface due to the adsorption of Ca^{2+},

HPO$_4^{2-}$ and PO$_4^{3-}$ ions by the remaining SCC on the surface (Fig. S3). In Fig. 5c, the characteristic peaks at 1558-1380 cm^{-1} of the porphyrin ring after an immersion of 24 h are generally shifted to the left, which might be attributed to the dementalization of SCC during the degradation process. The vibration peaks of HPO$_4^{2-}$ and PO$_4^{3-}$ ions appear at 1268-544 cm^{-1} [67], which can be confirmed by the XRD pattern of HA, Ca$_3$(PO$_4$)$_2$ and CaHPO$_4$. Corrosion products of Mg(OH)$_2$ was also not negligible.

XPS spectra of C 1s, Cu 2p and N 1s for (Ca–P/SCC)$_{10}$ coating with different immersion times are performed in Fig. 6. As shown in Fig. 6a, the C 1s spectrum has three peaks at 284.8, 286.5 and 288.4 eV, corresponding to the C–C and C–N bonds of the porphyrin ring and -COO$^-$ group. The Cu 2p spectra with three immersion time (Fig. 6b) show the same peaks of Cu^{2+} ions and coordinate Cu, confirming the demetalation of SCC [68]. That is, there are SCC and SCC without Cu existed during the degradation of the coating. In order to determine the change in the SCC structure in the (Ca–P/SCC)$_{10}$ coating as accurately as possible, XPS spectra of the N 1s with immersion time of 24, 50, 75, 170 and 300 h (Fig. 6c) are added. In the metalated molecules, the four N atoms are coordinated equally to the central ion and give rise to only one peak in the N 1s region, between the iminic (=N–, 398 eV) and pyrrolic (–NH–, 400 eV) peaks [69,70]. The three peak of N 1s spectra designates the existence of both metalized porphyrin and demetallized porphyrin. Otherwise, the pyrrolic peaks are shifted to the left, to varying degrees, before a soaking for 75 h. And the area of iminic and pyrrolic peaks are
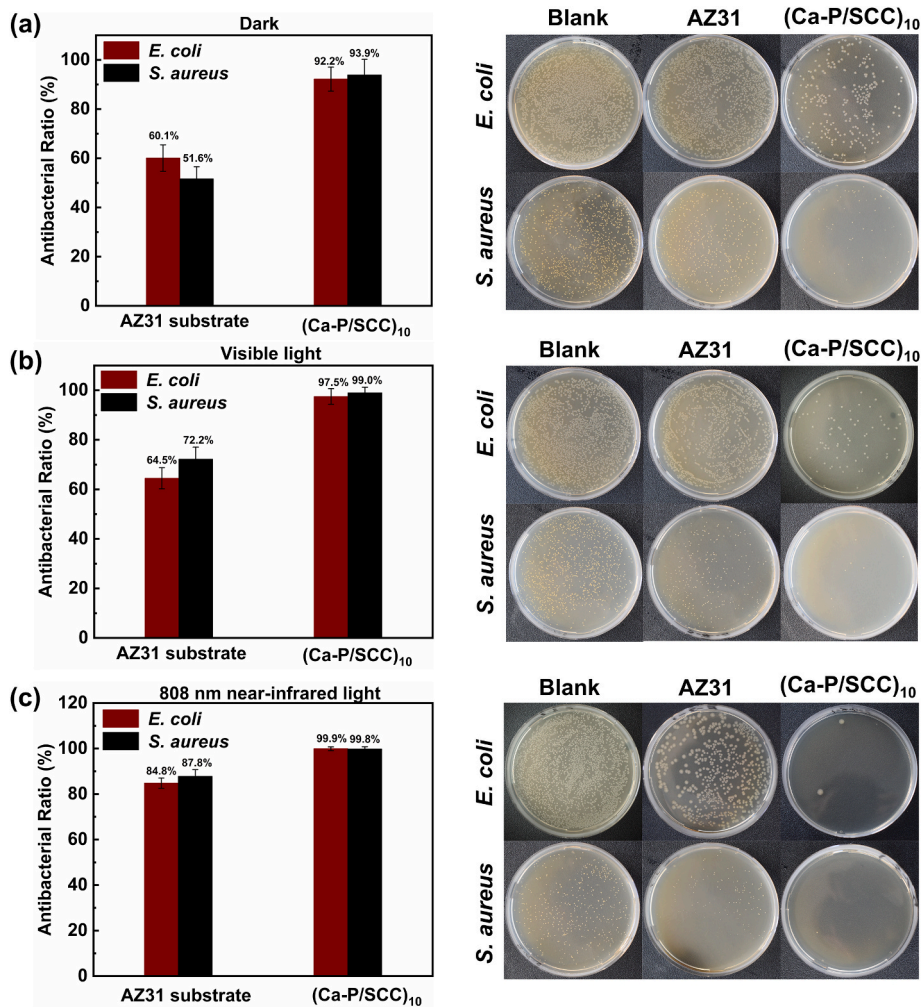
Fig. 7. Antibacterial ratio and colony images of samples against *S. aureus* and *E. coli* (a) in dark, under irradiation of (b) visible and (c) NIR light.
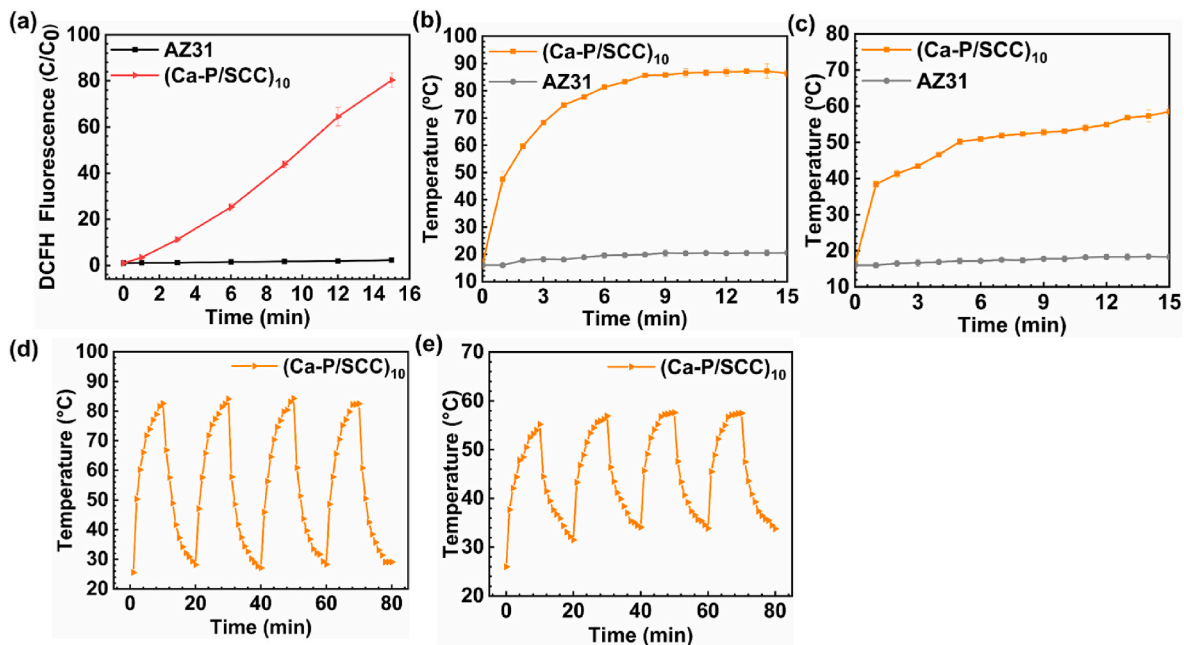

Fig. 8. (a) The amount of ROS released by the AZ31 substrate and (Ca–P/SCC)$_{10}$ coating; the temperature change curves of the AZ31 substrate and (Ca–P/SCC)$_{10}$ coating in (b) air and (c) HBSS; temperature change curves of the "on and off" performance for the (Ca–P/SCC)$_{10}$ coating in (d) air and (e) HBSS.

not equal, the pyrrolic peak area reaches the highest value at 50 h, and then decreases until it was equal to the area of iminic peak. The area of the N peak with metal ligands is always inversely proportional to the other two N peaks, indicating that when the number of demetallized porphyrin structure increases, the number of porphyrin structure with metal ligands would decreases, which may be attributed to the degradation of the coating during the soaking process. Note that, the proton concentration did not reach an equilibrium; and the coordination bond in the porphyrin structure is constantly changed [71].

Cu elemental content as function of immersion time is shown in Fig. 6d. In clinical practice, bacterial colonization adhesion and bacterial biofilm is the initial factor of bone implant infection, which usually occur within 24 h after surgery. Therefore, the antibacterial effect within 24 h is of great significance for the outbreak of postoperative infection of bone implants [72]. The Cu element release curve of the coating confirms that Cu element is gradually released from SCC; and during 0–170 h of immersion, especially within 24 h, the release rate sharply increases, due to the shedding of $(Ca-P/SCC)_{10}$ coating and many SCC molecules exposed to the solution cause demetalation, confirmed by the results of hydrogen evolution and immersion tests. After 170 h, the Cu element content is basically stable and most of the SCC molecules in $(Ca-P/SCC)_{10}$ coatings are completely demetallized, or reached a certain balance. The burst release time coincides with the outbreak period of postoperative infection, which improves the possibility of clinical application of the material.

3.4. Antibacterial ability

The antibacterial properties of AZ31 substrate and $(Ca-P/SCC)_{10}$ coating in dark are presented in Fig. 7, the antibacterial ratios of $(Ca-P/SCC)_{10}$ coating against *S. aureus* and *E. coli* are 93.9% and 92.2%, which are higher than that of AZ31 alloy of 51.6% and 60.1%, demonstrating the good inhibition of bacteria by Cu released during the degradation process of the $(Ca-P/SCC)_{10}$ coatings [73]. The antibacterial property of the bare AZ31 substrate can be ascribed to the released Mg^{2+} ions and increased pH value resulted from the corrosion process [74]. Due to the photosensitivity of SCC and degradation of $(Ca-P/SCC)_{10}$ coating, the ROS and Cu^{2+} ions can be released under the irradiation of visible light (1 W/cm^2) to inactivate bacteria, so that the antibacterial ratios of $(Ca-P/SCC)_{10}$ coating increased to 99.0% and 97.5%. While the increase in antibacterial activity of AZ31 substrate may be attributed to the highly localized electric field of plasmonic behavior under visible light [75]. The antibacterial efficacy against *S. aureus* and *E. coli* co-cultured with the $(Ca-P/SCC)_{10}$ coating reaches up to 99.8% and 99.9% under NIR irradiation, suggesting the synergetic effect of Cu, PTT and PDT. Note that, the antibacterial ratio and colony images of $(Ca-P)_{10}$ coating against *S. aureus* and *E. coli* are displayed in Fig. S4. The $(Ca-P)_{10}$ coating has no obvious antibacterial ability.

In order to explore the PDT effects of the $(Ca-P/SCC)_{10}$ coating, the change in fluorescence intensity of 2′,7′-dichlorofluorescein with different irradiation time is shown in Fig. 8a, in which C/C_0 means the ratio of the fluorescence intensity at the current moment to the initial fluorescence intensity. After an irradiation of 808 nm NIR light for 15 min, there is no ROS produced by the AZ31 alloy, a large amount of ROS generated via $(Ca-P/SCC)_{10}$ coating indicates a good PDT performance. Fig. 8b–e displays the photothermal property of $(Ca-P/SCC)_{10}$ coating under irradiation of 808 nm NIR light (1W/cm^2). The temperature of the $(Ca-P/SCC)_{10}$ coating reaches up to 87.4 and 58.5 °C in air and HBSS within 15 min; but no obvious changes in temperature on AZ31 alloy substrate, demonstrating a good PTT ability of the $(Ca-P/SCC)_{10}$ coating. As revealed in Fig. 8d and e, the temperature of $(Ca-P/SCC)_{10}$ coating exhibited a stable "on-off" behavior in air or HBSS, indicating an excellent photothermal stability. The corresponding thermal imager photos are exhibited in Fig. S5, the heat released by the sample in the air and in the solution is uniform, indicating the uniformity of $(Ca-P/SCC)_{10}$ coating.
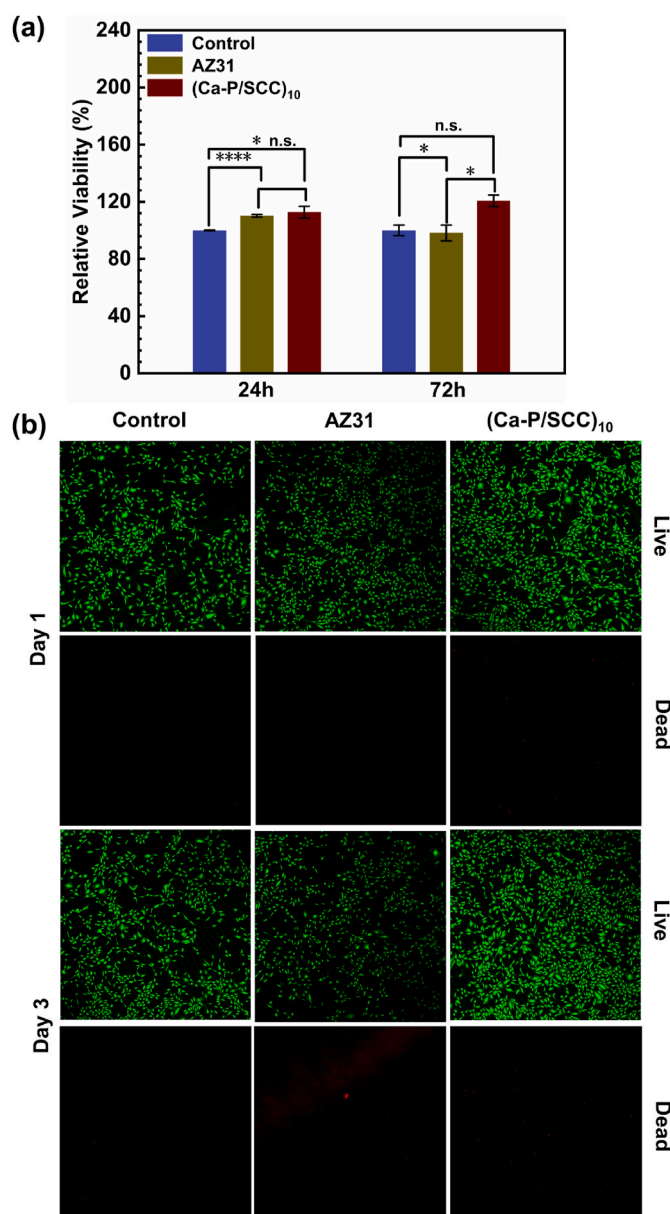

Fig. 9. (a) Cell viability of MC3T3-E1 cultured in different extracts prepared with negative control, AZ31 substrate and $(Ca-P/SCC)_{10}$ coating for 24 and 72 h. Statistically significant differences ($p^* < 0.05$, $p^{**} < 0.01$, $p^{***} < 0.001$, $p^{****} < 0.0001$); (b) Fluorescent images of MC3T3-E1after an incubation for 24 and 72 h in different extracts of the negative control, AZ31 substrate, and $(Ca-P/SCC)_{10}$ coating.

To determine the NIR photoabsorption capability of $(Ca-P/SCC)_{10}$ coating, the cooling curve of $(Ca-P/SCC)_{10}$ coating in Hank's solution is shown in Fig. S6a, and Fig. S6b is the graph of time (t) and -ln (θ). Because the temperature drops fast in the early stage of cooling and slow in the later stage, so a mid-term of the cooling process is conducted. After calculation, the photothermal conversion efficiency (η) of $(Ca-P/SCC)_{10}$ coating is 42.1%, in which m_{H_2O} is 2×10^{-3} kg ($c_{H_2O,p} = 4.2 \times 10^3$ J Kg^{-1} K^{-1}, $m_{scc} = 3 \times 10^{-3}$ kg, and $c_{scc} = 134.06$ J Kg^{-1} K^{-1}); hA equals to 0.018; $\Delta T_{max,mix}$ and $\Delta T_{max, H_2O}$ are 30.4 and 4.3 °C, respectively; I is 1 W; the area of light spot radiated on the $(Ca-P/SCC)_{10}$ coating is 1 cm^2; A_λ is 0.354.

3.5. Cytotoxicity

Cytocompatibility of the AZ31 substrate and $(Ca-P/SCC)_{10}$ coating is

characterized by the MTT method to detect the relative viablity of MC3T3-E1 cells in co-culture with the samples. The cell viabilities after 24 and 72 h incubation for pre-osteoblasts is exhibited in Fig. 9a. The extracts of $(Ca–P/SCC)_{10}$ coating significantly increase the viability of MC3T3-E1 cells to 112% and 120%, implying the active effect of the $(Ca–P/SCC)_{10}$ coating for promoting the growth of bone. The cell viability of AZ31 alloy after an incubation of 24 h goes up to 110%, indicating the good effect of Mg^{2+} ion on promoting osteogenic differentiation [76]. However, the viability decreases to 98% after a culture of 72 h, which might be ascribed to the high alkalinity resulted from the degradation of the AZ31 alloy [4]. Meanwhile, Live/Dead staining of osteoblasts after an incubation of 24 and 72 h could be seen in Fig. 9b. The cells for all samples performed generally healthy fusiform-like shape, widely spreading with respect to morphology, exhibiting an acceptable and enhanced cytocompatibility to osteoblasts.

4. Discussion

According to previous reports, substances which can prduce Cu^{2+} ions have been added to impart the antibacterial properties of the material, such as $CuSO_4$ [77], Cu monometallic [78], copper acetate [79], or CuO/Cu_2O [80]. There are, nevertheless, scarce reports on the applications of porphyrin on biodegradable metals.

Porphyrins are a class of tetrapyrrole compounds, which consist of a planar porphin core surrounded by substituent groups. The porphyrin ring has twenty-six π electrons, and is a highly conjugated system, determining that porphyrin has excellent electron transfer ability, PTT and PDT performance [81], and excellent biocompatibility [82]. They possess a high binding affnity to cellular components, membranes, proteins and DNA [83,84], can kill drug-resistant bacteria (e.g., MRSA) without destroying human cells [85].

There are many different mechanisms in which porphyrins are used to inactivate microorganisms and viruses. And the possibility of pathogens and bacteria gaining resistance is greatly reduced [86,87]. The structure of the SCC and Cu^{2+} ions is fully utilized on the $(Ca–P/SCC)_{10}$ coating, constructed a triple antibacterial system with good biocompatibility.

4.1. Coating formation and degradation mechism

SCC is a Cu-bearing porphyrin derivatives with good properties of transportation and storage of oxygen [88], transportation of electrons [89], light absorption and conversion [90] and photostability [71]. During the induction process of SCC, the carboxyl (-COO⁻) group in SCC can reduce the density of π electron cloud, resulting in the electron-withdrawing conjugation effect. Thus, SCC can firstly be adsorbed on the hydroxylated AZ31 substrate through electrostatic attraction. Subsequent nucleation and growth of Ca–P products show a cluster around the SCC (Fig. 2b). With the increase in the number of assembly layers, new SCC is attached to the sample surface by the electrostatic attraction in further to improve the thickness and compactness of the coating. Note that, although the density of functional groups in SCC is lower than that of DNA [9,10] and PAA [4] to induce Ca–P coating, the corrosion resistance is better than the DNA and PAA induced Ca–P coating, confirming the superiority of the LbL induction by SCC.

During the degradation process, based on the results of electrochemical and hydrogen evolution tests, $(Ca–P/SCC)_{10}$ coating has better electrochemical performance than $(Ca–P)_{10}$ coating and AZ31 substrate, and while $(Ca–P)_{10}$ coating shows the best corrosion resistance in the hydrogen evolution test. But before soaking for the first 20 h, the HER of $(Ca–P)_{10}$ coating was higher than that of $(Ca–P/SCC)_{10}$ coating and lower than AZ31 substrate, which is consistent with the results of electrochemical tests. This may be attributed to the fact that the compactness of $(Ca–P)_{10}$ coating is not as good as that of $(Ca–P/SCC)_{10}$ coating. Obvious corrosion cracks appear on the surface of $(Ca–P/SCC)_{10}$ coating

after being immersed for 24 h (Fig. 5). As the immersion time is prolonged, a large amount of Cu^{2+} ions produced by the demetallization reaction of SCC attacks the substrate together with the aggressive ions (Fig. 6d), and galvanic corrosion occurs [62], which corresponds to the sudden and rapid rise of HER at the immersion time of 50 h in Fig. 4i.

Thus, the degradation mechanism of the $(Ca–P/SCC)_{10}$ coating can be divided into four steps:

(1) After the sample is exposed to the HBSS solution, the dense layered $(Ca–P/SCC)_{10}$ coating provides a physical barrier for the AZ31 substrate, hindering the attack of solute ions on the AZ31 substrate.
(2) Subsequently, the $(Ca–P/SCC)_{10}$ coating gradually degrades, and the SCC in the $(Ca–P/SCC)_{10}$ coating undergoes a demetallization reaction to release Cu^{2+} ions.
(3) As the immersion time increases, obvious corrosion defects occur resulted from galvanic corrosion between the Al–Mn and α-Mg phases in AZ31 substrate, and the Cu^{2+} ions and Mg substrates. The degradation rate of the coating reaches to the maximum in this process.
(4) Finally, the deposition of corrosion products fills in the corrosion defects until the degradation of the coating and the formation of the products film reach a relative balance.

Therefore, the long term corrosion protection of the $(Ca–P/SCC)_{10}$ coating is limited, which should be improved in further.

4.2. Ternary antibacterial mechanism

In vitro antibacterial activity of the $(Ca–P/SCC)_{10}$ coating varies with the changing environment. In dark, the released Cu^{2+} ion from the $(Ca–P/SCC)_{10}$ coating during the degradation process exerts antibacterial effect, based on Cu^{2+} ion can destroy the bacterial cell membrane to its inactivation [91]. Otherwise, as the coating degrades, the Mg^{2+} ions also are released from the substrate, cooperating with the enhanced alkalinity to inhibit bacteria [92].

Under the irradiation of visible light, the SCC is excited by the light of a specific wavelength, undergoing a photo-oxidation reaction in two cases:

Type I: photooxidation mechanism [93],

Porphyrin absorbs light into singlet excited state (1 PS*), once in a singlet excited state, PS molecules can be converted to a triplet excited state (3 PS*) by intersystem crossing (ISC) [94]:

$$P(S_0) \rightarrow {}^1PS* \tag{10}$$

$$1\,PS* + ISC \rightarrow 3\,PS* \tag{11}$$

$${}^3PS* + D \rightarrow PS^{\bullet-} + D^{\bullet+} \tag{12}$$

Radical-anion of the porphyrin ($PS^{\bullet-}$) may also transfer electrons to O_2 with formation of superoxide-anion radical $O_2^{\bullet-}$:

$$PS^{\bullet-} + O_2 \rightarrow PS + O_2^{\bullet-} \tag{13}$$

Alternatively, reactive oxygen species (ROS), e. g. singlet oxygen is produced according to type II: photooxidation mechanism, the semi-reduced PS radical can react with electron acceptors, such as oxygen, regenerating the PS [95].

$$^3PS* + O_2 \rightarrow {}^1O_2 + PS \tag{14}$$

Under the irradiation of NIR, a new PTT mechanism can be concluded as the light absorbed by the SCC from the target site to generate heat. In order to avoid damage to healthy cells, a photosensitizer with high absorption and photothermal conversion efficiency under NIR light is necessary. Note that, bacteria and cancer cells can be killed when the temperature of PTT exceeds 40 °C. The inactivation process needs to last 6–72 h when the temperature is 40–41 °C, and
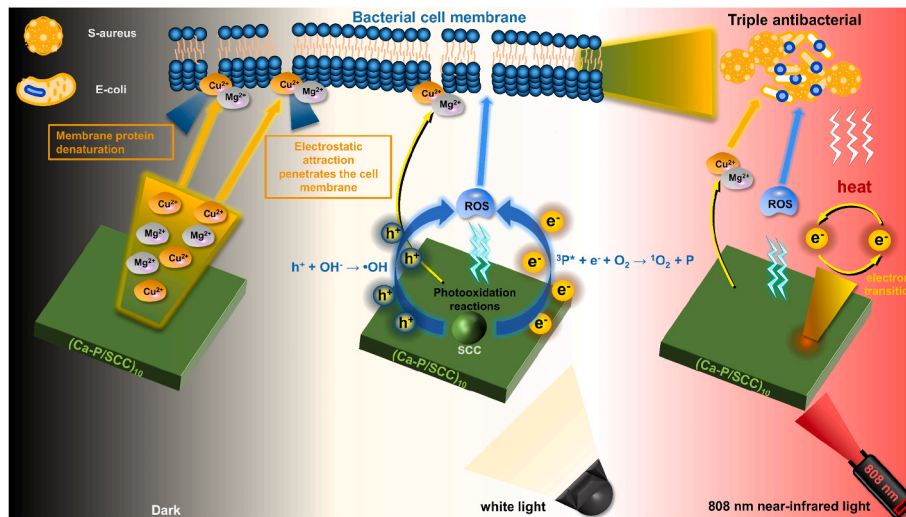
Fig. 10. Diagram of antibacterial mechanisms for (Ca–P/SCC)$_{10}$ coating in different environment.

15–60 min when the temperature is 42–45 °C. When the temperature reaches over 50 °C, the inactivation process will be shortened to 4–6 min [96]. Thus, experiments have proved the high-efficiency triple antibacterial (Fig. 10) properties of the (Ca–P/SCC)$_{10}$ coating, and the (Ca–P/SCC)$_{10}$ coating may be a candidate in the treatment of cancer.

5. Conclusions

A (Ca–P/SCC)$_{10}$ coating has been successfully prepared on AZ31 alloy by LbL assembly.

(1) Dense lamellar or leaf-like (Ca–P/SCC)$_{10}$ coating is mainly composed of CaHPO$_4\cdot$H$_2$O, Ca$_3$(PO$_4$)$_2$, HA and Mg(OH)$_2$, and SCC facilitates the initiation of Ca–P layer. The corrosion current density decreased one order of magnitude from AZ31 substrate (5.45×10^{-6} A cm^{-2}) and (Ca–P)$_{10}$ coating (7.23×10^{-6} A cm^{-2}) to (Ca–P/SCC)$_{10}$ coating (1.35×10^{-7} A cm^{-2}), indicating the (Ca–P/SCC)$_{10}$ coating has a good corrosion resistance. But the release of Cu^{2+} ions leads to galvanic corrosion and accelerates corrosion rate during the coating degradation.

(2) The antibacterial efficacy of the (Ca–P/SCC)$_{10}$ coating under the irradiation of NIR light reaches as high as 99.8% and 99.9% against *S. aureus* and *E. coli*, respectively, which is attributable to the Cu bearing (Ca–P/SCC)$_{10}$ coating with excellent photodynamic, photothermal properties and photothermal stability. A triple antibacterial mechanism is proposed.

(3) The MC3T3-E1 pre-osteoblasts cells for (Ca–P/SCC)$_{10}$ coating reveals generally healthy fusiform-like shape, widely spreading with respect to morphology, exhibiting an enhanced cytocompatibility to osteoblasts. The (Ca–P/SCC)$_{10}$ coating shows great potential for applications on biodegradable Mg alloys.

CRediT authorship contribution statement

Zhen-Yu Zhang: Conceptualization, Methodology, Investigation, Visualization, Software, Formal analysis, Data curation, Writing – original draft, preparation, Writing – review & editing. **Yan-Lin An:** Visualization, Investigation. **Xiao-Shi Wang:** Visualization, Investigation. **Lan-Yue Cui:** Methodology, Investigation, Writing – review & editing, Supervision, Funding acquisition. **Shuo-Qi Li:** Writing – review & editing, Supervision. **Cheng-Bao Liu:** Writing – review & editing, Supervision. **Yu-Hong Zou:** Supervision. **Fen Zhang:** Supervision. **Rong-Chang Zeng:** Methodology, Writing – review & editing, Supervision, Funding acquisition.

Declaration of competing interest

The authors declare that they have no known competing financial interests or personal relationships that could have appeared to influence the work reported in this paper.

Appendix A. Supplementary data

Supplementary data to this article can be found online at https://doi.org/10.1016/j.bioactmat.2022.01.050.

References

[1] H.M. Kang, B.G. Yang, K.Y. Zhang, Q. Pan, W.H. Yuan, G. Li, L.M. Bian, Immunoregulation of macrophages by dynamic ligand presentation via ligand-cation coordination, Nat. Commun. 10 (2019) 1696, https://doi.org/10.1038/s41467-019-09733-6.

[2] C. Liu, Z. Ren, Y. Xu, S. Pang, X. Zhao, Y. Zhao, Biodegradable magnesium alloys developed as bone repair materials: a review, Scanning (2018), 9216314, https://doi.org/10.1155/2018/9216314, 2018.

[3] L. Malladi, A. Mahapatro, A.S. Gomes, Fabrication of magnesium-based metallic scaffolds for bone tissue engineering, Mater. Technol. 33 (2) (2018) 173–182, https://doi.org/10.1080/10667857.2017.1404278.

[4] L.Y. Cui, S.C. Cheng, L.X. Liang, J.C. Zhang, S.Q. Li, Z.L. Wang, R.C. Zeng, In vitro corrosion resistance of layer-by-layer assembled polyacrylic acid multilayers induced Ca-P coating on magnesium alloy AZ31, Bioact. Mater. 5 (1) (2020) 153–163, https://doi.org/10.1016/j.bioactmat.2020.02.001.

[5] L. Wu, X. Ding, Z. Zheng, A. Tang, G. Zhang, A. Atrens, F. Pan, Doubly-doped Mg-Al-Ce-V$_2$O$_7$$^{4-}$ LDH composite film on magnesium alloy AZ31 for anticorrosion, J. Mater. Sci. Technol. 64 (2021) 66–72, https://doi.org/10.1016/j.jmst.2019.09.031.

[6] M.A. Surmeneva, A.I. Tyurin, T.M. Mukhametkaliyev, T.S. Pirozhkova, I.A. Shuvarin, M.S. Syrtanov, R.A. Surmenev, Enhancement of the mechanical properties of AZ31 magnesium alloy via nanostructured hydroxyapatite thin films fabricated via radio-frequency magnetron sputtering, J. Mech. Behav. Biomed. Mater. 46 (2015) 127–136, https://doi.org/10.1016/j.jmbbm.2015.02.025.

[7] M.A. Surmeneva, A.A. Ivanova, Q.M. Tian, R. Pittman, W.S. Jiang, J.J. Lin, H.N. H. Liu, R.A. Surmenev, Bone marrow derived mesenchymal stem cell response to the RF magnetron sputter deposited hydroxyapatite coating on AZ91 magnesium alloy, Mater. Chem. Phys. 221 (2019) 89–98, https://doi.org/10.1016/j.matchemphys.2018.09.030.

[8] J.P. Han, C. Blawert, S.W. Tang, J.J. Yang, J. Hu, M.L. Zheludkevich, Formation and corrosion behaviors of calcium phosphate coatings on plasma electrolytic oxidized Mg under changing chemical environment, Surf. Coating. Technol. 412 (2021), https://doi.org/10.1016/j.surfcoat.2021.127030.

[9] P. Liu, J.M. Wang, X.T. Yu, X.B. Chen, S.Q. Li, D.C. Chen, S.K. Guan, R.C. Zenga, L. Y. Cui, Corrosion resistance of bioinspired DNA-induced Ca-P coating on biodegradable magnesium alloy, J. Magnes. Alloy. 7 (1) (2019) 144–154, https://doi.org/10.1016/j.jma.2019.01.004.

[10] Z.Y. Zhang, D. Wang, L.X. Liang, S.C. Cheng, L.Y. Cui, S.Q. Li, Z.L. Wang, R.C. Zeng, Corrosion resistance of Ca-P coating induced by layer-by-layer assembled polyvinylpyrrolidone/DNA multilayer on magnesium AZ31 alloy, Front. Mater. Sci. 15 (3) (2021) 391–405, https://doi.org/10.1007/s11706-021-0560-x.

[11] D.W. Grainger, H.C. van der Mei, P.C. Jutte, J.J. van den Dungen, M.J. Schultz, B. F. van der Laan, S.A. Zaat, H.J. Busscher, Critical factors in the translation of improved antimicrobial strategies for medical implants and devices, Biomaterials 34 (37) (2013) 9237–9243, https://doi.org/10.1016/j.biomaterials.2013.08.043.

[12] X.J. Ji, L. Gao, J.C. Liu, J. Wang, Q. Cheng, J.P. Li, S.Q. Li, K.Q. Zhi, R.C. Zeng, Z. L. Wang, Corrosion resistance and antibacterial properties of hydroxyapatite coating induced by gentamicin-loaded polymeric multilayers on magnesium alloys, Colloids Surf. B Biointerfaces 179 (2019) 429–436, https://doi.org/10.1016/j.colsurfb.2019.04.029.

[13] X.J. Ji, L. Gao, J.C. Liu, R.Z. Jiang, F.Y. Sun, L.Y. Cui, S.Q. Li, K.Q. Zhi, R.C. Zeng, Z.L. Wang, Corrosion resistance and antibacterial activity of hydroxyapatite coating induced by ciprofloxacin-loaded polymeric multilayers on magnesium alloy, Prog. Org. Coating 135 (2019) 465–474, https://doi.org/10.1016/j.porgcoat.2019.06.048.

[14] T.F. Wang, G.Y. Ni, T. Furushima, H. Diao, P.P. Zhang, S. Chen, C.E. Fogarty, Z. Y. Jiang, X.S. Liu, H.J. Li, Mg alloy surface immobilised with caerin peptides acquires enhanced antibacterial ability and putatively improved corrosion resistance, Mater. Sci. Eng. C-Mater. Biol. Appl. 121 (2021), 111819, https://doi.org/10.1016/j.msec.2020.111819.

[15] P. Kumar, S. Dev, S.S. Dhayal, V. Acharya, S. Kumar, S. Kumar, N. Singh, R. Dhar, Synergistic effect of Mg and Se co-doping on the structural, optical and anti-bacterial activity of ZnO thin films, Inorg. Chem. Commun. 131 (2021), 108801, https://doi.org/10.1016/j.inoche.2021.108801.

[16] C.L. Zhao, P. Hou, J.H. Ni, P. Han, Y.M. Chai, X.N. Zhang, Ag-incorporated FHA coating on pure Mg: degradation and in vitro antibacterial properties, ACS Appl. Mater. Interfaces 8 (8) (2016) 5093–5103, https://doi.org/10.1021/acsami.5b10825.

[17] Y.H. Zou, J. Wang, L.Y. Cui, R.C. Zeng, Q.Z. Wang, Q.X. Han, J. Qiu, X.B. Chen, D. C. Chen, S.K. Guan, Y.F. Zheng, Corrosion resistance and antibacterial activity of zinc-loaded montmorillonite coatings on biodegradable magnesium alloy AZ31, Acta Biomater. 98 (2019) 196–214, https://doi.org/10.1016/j.actbio.2019.05.069.

[18] L.Y. Cui, S.D. Gao, P.P. Li, R.C. Zeng, F. Zhang, S.Q. Li, E.H. Han, Corrosion resistance of a self-healing micro-arc oxidation/polymethyltrimethoxysilane composite coating on magnesium alloy AZ31, Corrosion Sci. 118 (2017) 84–95, https://doi.org/10.1016/j.corsci.2017.01.025.

[19] Y. Shao, R.C. Zeng, S.Q. Li, L.Y. Cui, Y.H. Zou, S.K. Guan, Y.F. Zheng, Advance in antibacterial magnesium alloys and surface coatings on magnesium alloys: a review, Acta Metall. Sin.-Engl. Lett. 33 (5) (2020) 615–629, https://doi.org/10.1007/s40195-020-01044-w.

[20] Z.Z. Yin, W.C. Qi, R.C. Zeng, X.B. Chen, C.D. Gu, S.K. Guan, Y.F. Zheng, Advances in coatings on biodegradable magnesium alloys, J. Magnes. Alloy. 8 (1) (2020) 42–65, https://doi.org/10.1016/j.jma.2019.09.008.

[21] M.P. Romero, V.S. Marangoni, C.G. de Faria, I.S. Leite, C. Silva, C.M. Maroneze, M. A. Pereira-da-Silva, V.S. Bagnato, N.M. Inada, Graphene oxide mediated broad-spectrum antibacterial based on bimodal action of photodynamic and photothermal effects, Front. Microbiol. 10 (2020) 2995, https://doi.org/10.3389/fmicb.2020.02995.

[22] L. Beytollahi, M. Pourhajibagher, N. Chiniforush, R. Ghorbanzadeh, R. Raoofian, B. Pourakbari, A. Bahador, The efficacy of photodynamic and photothermal therapy on biofilm formation of Streptococcus mutans: an in vitro study, Photodiagnosis Photodyn. Ther. 17 (2017) 56–60, https://doi.org/10.1016/j.pdpdt.2016.10.006.

[23] R. Su, H. Yan, P. Li, B. Zhang, Y. Zhang, W. Su, Photo-enhanced antibacterial activity of polydopamine-curcumin nanocomposites with excellent photodynamic and photothermal abilities, Photodiagnosis Photodyn. Ther. 35 (2021) 102417, https://doi.org/10.1016/j.pdpdt.2021.102417.

[24] W. Ren, Y. Yan, L. Zeng, Z. Shi, A. Gong, P. Schaaf, D. Wang, J. Zhao, B. Zou, H. Yu, G. Chen, E.M. Brown, A. Wu, A near infrared light triggered hydrogenated black TiO2 for cancer photothermal therapy, Adv. Healthc. Mater. 4 (10) (2015) 1526–1536, https://doi.org/10.1002/adhm.201500273.

[25] C. Mao, Y. Xiang, X. Liu, Z. Cui, X. Yang, Z. Li, S. Zhu, Y. Zheng, K.W.K. Yeung, S. Wu, Repeatable photodynamic therapy with triggered signaling pathways of fibroblast cell proliferation and differentiation to promote bacteria-accompanied wound healing, ACS Nano 12 (2) (2018) 1747–1759, https://doi.org/10.1021/acsnano.7b08500.

[26] M.B. Vrouenraets, G.W. Visser, G.B. Snow, G.A. van Dongen, Basic principles, applications in oncology and improved selectivity of photodynamic therapy, Anticancer Res. 23 (1B) (2003) 505–522, https://doi.org/10.1121/1.2890703.

[27] M. Hockel, P. Vaupel, Tumor hypoxia: definitions and current clinical, biologic, and molecular aspects, JNCI-J. Natl. Cancer Inst. 93 (4) (2001) 266–276, https://doi.org/10.1093/jnci/93.4.266.

[28] J.R. Peng, Q. Yang, W.T. Li, L.W. Tan, Y. Xiao, L.J. Chen, Y. Hao, Z.Y. Qian, Erythrocyte-membrane-Coated prussian blue/manganese dioxide nanoparticles as H2O2-responsive oxygen generators to enhance cancer chemotherapy/photothermal therapy, ACS Appl. Mater. Interfaces 9 (51) (2017) 44410–44422, https://doi.org/10.1021/acsami.7b17022.

[29] M. Nikfarjam, V. Muralidharan, C. Christophi, Mechanisms of focal heat destruction of liver tumors, J. Surg. Res. 127 (2) (2005) 208–223, https://doi.org/10.1016/j.jss.2005.02.009.

[30] H.V. Anderson, G.S. Zaatari, G.S. Roubin, P.P. Leimgruber, A.R. Gruentzig, Steerable fiberoptic catheter delivery of laser energy in atherosclerotic rabbits, Am. Heart J. 111 (6) (1986) 1065–1072, https://doi.org/10.1016/0002-8703(86)90007-4.

[31] F. Perreault, A.F. de Faria, S. Nejati, M. Elimelech, Antimicrobial properties of graphene oxide nanosheets: why size matters, ACS Nano 9 (7) (2015) 7226–7236, https://doi.org/10.1021/acsnano.5b02067.

[32] Y. Duan, H. Yang, J. Gao, D. Wei, Y. Wang, J. Wang, X. Zhang, J. Zhang, K. Ge, X. Wu, J. Chang, Immune modulator and low-temperature PTT-induced synergistic immunotherapy for cancer treatment, ACS Appl. Bio Mater. 4 (2) (2021) 1524–1535, https://doi.org/10.1021/acsabm.0c01397.

[33] Y. Li, X. Liu, L. Tan, Z. Cui, X. Yang, Y. Zheng, K.W.K. Yeung, P.K. Chu, S. Wu, Rapid sterilization and accelerated wound healing using Zn^{2+} and graphene oxide modified g-C$_3$N$_4$ under dual light irradiation, Adv. Funct. Mater. 28 (30) (2018), https://doi.org/10.1002/adfm.201800299.

[34] E.H. Cho, S.H. Chae, K. Kim, S.J. Lee, J. Joo, Photovoltaic characteristics of organic solar cells using Zn–porphyrin derivatives with controlled π-conjugation structures, Synth. Met. 162 (9–10) (2012) 813–819, https://doi.org/10.1016/j.synthmet.2012.03.007.

[35] H.J. Son, S. Jin, S. Patwardhan, S.J. Wezenberg, N.C. Jeong, M. So, C.E. Wilmer, A. A. Sarjeant, G.C. Schatz, R.Q. Snurr, O.K. Farha, G.P. Wiederrecht, J.T. Hupp, Light-harvesting and ultrafast energy migration in porphyrin-based metal-organic frameworks, J. Am. Chem. Soc. 135 (2) (2013) 862–869, https://doi.org/10.1021/ja310596a.

[36] C.S. Jin, J.F. Lovell, J. Chen, G. Zheng, Ablation of hypoxic tumors with dose-equivalent photothermal, but not photodynamic, therapy using a nanostructured porphyrin assembly, ACS Nano 7 (3) (2013) 2541–2550, https://doi.org/10.1021/nn3058642.

[37] J.T. Robinson, S.M. Tabakman, Y. Liang, H. Wang, H.S. Casalongue, D. Vinh, H. Dai, Ultrasmall reduced graphene oxide with high near-infrared absorbance for photothermal therapy, J. Am. Chem. Soc. 133 (17) (2011) 6825–6831, https://doi.org/10.1021/ja2010175.

[38] T. Sakurai, S. Sakaguchi, Y. Takeshita, K. Kayama, A. Horio, M. Sugimoto, T. Yamaki, A. Chiba, Y. Saitoh, L.B.V.S. Garimella, D.K. Avasthi, S. Seki, Porphyrin nanowire bundles for efficient photoconductivity, photoemission, and generation of singlet oxygens toward photodynamic therapy, ACS Appl. Nano Mater. 3 (6) (2020) 6043–6053, https://doi.org/10.1021/acsanm.0c01242.

[39] X.T. Tian, P.P. Cao, H. Zhang, Y.H. Li, X.B. Yin, GSH-activated MRI-guided enhanced photodynamic- and chemo-combination therapy with a MnO$_2$-coated porphyrin metal organic framework, Chem. Commun. 55 (44) (2019) 6241–6244, https://doi.org/10.1039/c9cc01957j.

[40] C.S. Jin, J.F. Lovell, J. Chen, G. Zheng, Ablation of hypoxic tumors with dose-equivalent photothermal, but not photodynamic, therapy using a nanostructured porphyrin assembly, ACS Nano 7 (3) (2013) 2541–2550, https://doi.org/10.1021/nn3058642.

[41] H. Chen, A. Ma, T. Yin, Z. Chen, R. Liang, H. Pan, X. Shen, M. Zheng, L. Cai, In situ photocatalysis of TiO-Porphyrin-Encapsulated nanosystem for highly efficient oxidative damage against hypoxic tumors, ACS Appl. Mater. Interfaces 12 (11) (2020) 12573–12583, https://doi.org/10.1021/acsami.0c00921.

[42] J. Das, A. Samadder, J. Mondal, S.K. Abraham, A.R. Khuda-Bukhsh, Nano-encapsulated chlorophyllin significantly delays progression of lung cancer both in in vitro and in vivo models through activation of mitochondrial signaling cascades and drug-DNA interaction, Environ. Toxicol. Pharmacol. 46 (2016) 147–157, https://doi.org/10.1016/j.etap.2016.07.006.

[43] M. Chu, H. Li, Q. Wu, F. Wo, D. Shi, Pluronic-encapsulated natural chlorophyll nanocomposites for in vivo cancer imaging and photothermal/photodynamic therapies, Biomaterials 35 (29) (2014) 8357–8373, https://doi.org/10.1016/j.biomaterials.2014.05.049.

[44] D. Pemmaraju, T. Appidi, G. Minhas, S.P. Singh, N. Khan, M. Pal, R. Srivastava, A. K. Rengan, Chlorophyll rich biomolecular fraction of A. cadamba loaded into polymeric nanosystem coupled with Photothermal Therapy: a synergistic approach for cancer theranostics, Int. J. Biol. Macromol. 110 (2018) 383–391, https://doi.org/10.1016/j.ijbiomac.2017.09.084.

[45] M.J. Malone-Povolny, S.E. Maloney, M.H. Schoenfisch, Nitric oxide therapy for diabetic wound healing, Adv. Healthcare Mater. 8 (12) (2019), e1801210, https://doi.org/10.1002/adhm.201801210.

[46] T. Liang, Y.P. Wang, L.L. Zeng, Y.Z. Liu, L.P. Qiao, S.F. Zhang, R.F. Zhao, G.Q. Li, R. F. Zhang, J.H. Xiang, F.C. Xiong, A. Shanaghi, H.B. Pan, Y. Zhao, Copper-doped 3D porous coating developed on Ti-6Al-4V alloys and its in vitro long-term antibacterial ability, Appl. Surf. Sci. 509 (2020), 144717, https://doi.org/10.1016/j.apsusc.2019.144717.

[47] S. Yu, G. Li, R. Liu, D. Ma, W. Xue, Dendritic Fe$_3$O$_4$@Poly(dopamine)@PAMAM nanocomposite as controllable NO-releasing material: a synergistic photothermal and NO antibacterial study, Adv. Funct. Mater. 28 (20) (2018), https://doi.org/10.1002/adfm.201707440.

[48] T. Xi, M.B. Shahzad, D. Xu, Z. Sun, J. Zhao, C. Yang, M. Qi, K. Yang, Effect of copper addition on mechanical properties, corrosion resistance and antibacterial property of 316L stainless steel, Mater. Sci. Eng. C-Mater. Biol. Appl. 71 (2017) 1079–1085, https://doi.org/10.1016/j.msec.2016.11.022.

[49] F.S. da Silva, A.C.A. de Paula e Silva, P.A. Barbugli, N. Cinca, S. Dosta, I.G. Cano, J. M. Guilemany, C.E. Vergani, A.V. Benedetti, Anti-biofilm activity and in vitro biocompatibility of copper surface prepared by cold gas spray, Surf. Coating. Technol. 411 (2021), 126981, https://doi.org/10.1016/j.surfcoat.2021.126981.

[50] J. Xiao, Y. Zhu, S. Huddleston, P. Li, B. Xiao, O.K. Farha, G.A. Ameer, Copper metal-organic framework nanoparticles stabilized with folic acid improve wound healing in diabetes, ACS Nano 12 (2) (2018) 1023–1032, https://doi.org/10.1021/acsnano.7b01850.

[51] A.P. Kornblatt, V.G. Nicoletti, A. Travaglia, The neglected role of copper ions in wound healing, J. Inorg. Biochem. 161 (2016) 1–8, https://doi.org/10.1016/j.jinorgbio.2016.02.012.

[52] G.Y. Koga, B. Albert, V. Roche, R.P. Nogueira, A comparative study of mild steel passivation embedded in Belite-Ye'elimite-Ferrite and Porland cement mortars, Electrochim. Acta 261 (2018) 66–77, https://doi.org/10.1016/j.electacta.2017.12.128.

[53] Y. Xiang, C. Mao, X. Liu, Z. Cui, D. Jing, X. Yang, Y. Liang, Z. Li, S. Zhu, Y. Zheng, K.W.K. Yeung, D. Zheng, X. Wang, S. Wu, Rapid and superior bacteria killing of carbon quantum dots/ZnO decorated injectable folic acid-conjugated PDA hydrogel through dual-light triggered ROS and membrane permeability, Small 15 (22) (2019), e1900322, https://doi.org/10.1002/smll.201900322.

[54] Y. Liu, K. Ai, J. Liu, M. Deng, Y. He, L. Lu, Dopamine-melanin colloidal nanospheres: an efficient near-infrared photothermal therapeutic agent for in vivo cancer therapy, Adv. Mater. 25 (9) (2013) 1353–1359, https://doi.org/10.1002/adma.201204683.

[55] Y. Zhao, M.I. Jamesh, W.K. Li, K.W.K. Yeung, P.K. Chu, Enhanced antimicrobial properties, cytocompatibility, and corrosion resistance of plasma-modified biodegradable magnesium alloys, Acta Biomater. 10 (1) (2014) 544–556, https://doi.org/10.1016/j.actbio.2013.10.012.

[56] G.Y. Wang, W.W. Yan, X.H. Zhang, W.J. Ruan, Z.A. Zhu, Synthesis and spectral properties of salen-porphyrin type homo- and hetero-binuclear complexes with pi-conjugate configuration, Acta Phys. Chim. Sin. 28 (12) (2012) 2774–2782, https://doi.org/10.3866/PKU.WHXB201209261.

[57] D.D. La, H.P.N. Thi, Y.S. Kim, A. Rananaware, S.V. Bhosale, Facile fabrication of Cu (II)-porphyrin MOF thin films from tetrakis(4-carboxyphenyl) porphyrin and Cu (OH)(2) nanoneedle array, Appl. Surf. Sci. 424 (2017) 145–150, https://doi.org/10.1016/j.apsusc.2017.01.110.

[58] S.A. Gungor, M. Kose, F. Tumer, M. Tumer, Photoluminescence, electrochemical, SOD activity and selective chemosensor properties of novel asymmetric porphyrin-Schiff base compounds, Dyes Pigments 130 (2016) 37–53, https://doi.org/10.1016/j.dyepig.2016.03.007.

[59] Y. Fazaeli, S. Feizi, A.R. Jalilian, A. Hejrani, Grafting of Cu-64 -TPPF20 porphyrin complex on Functionalized nano-porous MCM-41 silica as a potential cancer imaging agent, Appl. Radiat. Isot. 112 (2016) 13–19, https://doi.org/10.1016/j.apradiso.2016.03.003.

[60] S.M. Pu, M.Y. Chen, Y.Q. Chen, W.T. Zhang, H. Soliman, A. Qu, Q.J. Liu, X. Tang, N. Huang, G.J. Wan, Zirconium ions integrated in 1-hydroxyethylidene-1,1-diphosphonic acid (HEDP) as a metalorganic-like calcium coating on biodegradable magnesium for corrosion control, Corrosion Sci. 144 (2018) 277–287, https://doi.org/10.1016/j.corsci.2018.09.003.

[61] C.Y. Li, X.L. Fan, L.Y. Cui, R.C. Zeng, Corrosion resistance and electrical conductivity of a nano ATO-doped MAO/methyltrimethoxysilane composite coating on magnesium alloy AZ31, Corrosion Sci. 168 (2020), https://doi.org/10.1016/j.corsci.2020.108570.

[62] X. Shi, Y. Wang, H. Li, S. Zhang, R. Zhao, G. Li, R. Zhang, Y. Sheng, S. Cao, Y. Zhao, L. Xu, Y. Zhao, Corrosion resistance and biocompatibility of calcium-containing coatings developed in near-neutral solutions containing phytic acid and phosphoric acid on AZ31B alloy, J. Alloys Compd. 823 (2020), https://doi.org/10.1016/j.jallcom.2020.153721.

[63] G.J. Gao, M.Q. Zeng, E.L. Zhang, R.C. Zeng, L.Y. Cui, D.k. Xu, F.Q. Wang, M. B. Kannan, Dealloying corrosion of anodic and nanometric Mg41Nd5 in solid solution-treated Mg-3Nd-1Li-0.2Zn alloy, J. Mater. Sci. Technol. 83 (2021) 161–178, https://doi.org/10.1016/j.jmst.2020.12.049.

[64] G. Zhang, L. Wu, A. Tang, Y. Ma, G.-L. Song, D. Zheng, B. Jiang, A. Atrens, F. Pan, Active corrosion protection by a smart coating based on a MgAl-layered double hydroxide on a cerium-modified plasma electrolytic oxidation coating on Mg alloy AZ31, Corrosion Sci. 139 (2018) 370–382, https://doi.org/10.1016/j.corsci.2018.05.010.

[65] M.J. Anjum, J. Zhao, V. Zahedi Asl, G. Yasin, W. Wang, S. Wei, Z. Zhao, W. Qamar Khan, In-situ intercalation of 8-hydroxyquinoline in Mg-Al LDH coating to improve the corrosion resistance of AZ31, Corrosion Sci. 157 (2019) 1–10, https://doi.org/10.1016/j.corsci.2019.05.022.

[66] G. Liu, S. Tang, D. Li, J. Hu, Self-adjustment of calcium phosphate coating on micro-arc oxidized magnesium and its influence on the corrosion behaviour in simulated body fluids, Corrosion Sci. 79 (2014) 206–214, https://doi.org/10.1016/j.corsci.2013.11.011.

[67] R.J. Kavitha, K. Ravichandran, T. Narayanan, Deposition of strontium phosphate coatings on magnesium by hydrothermal treatment: characteristics, corrosion resistance and bioactivity, J. Alloys Compd. 745 (2018) 725–743, https://doi.org/10.1016/j.jallcom.2018.02.200.

[68] Y.N. Hua, Y. Shen, K. Li, J.Y. Wang, Y.S. Chan, Y.X. Chen, C. Fu, X.M. Li, Ieee, Studies on XPS Valence State Analysis of Copper Materials, 37th IEEE International Electronics Manufacturing Technology Conference (IEMT)/18th Electronics Materials and Packaging, (EMAP) Conference, Malaysia, 2016.

[69] F. Klappenberger, A. Weber-Bargioni, W. Auwarter, M. Marschall, A. Schiffrin, J. V. Barth, Temperature dependence of conformation, chemical state, and metal-directed assembly of tetrapyridyl-porphyrin on Cu(111), J. Chem. Phys. 129 (21) (2008) 214702, https://doi.org/10.1063/1.3021291.

[70] K. Diller, A.C. Papageorgiou, F. Klappenberger, F. Allegretti, J.V. Barth, W. Auwarter, In vacuo interfacial tetrapyrrole metallation, Chem. Soc. Rev. 45 (6) (2016) 1629–1656, https://doi.org/10.1039/c5cs00207a.

[71] C.C. Fernandez, M. Franke, H.P. Steinruck, O. Lytken, F.J. Williams, Demetalation of surface porphyrins at the solid-liquid interface, Langmuir 37 (2) (2021) 852–857, https://doi.org/10.1021/acs.langmuir.0c03197.

[72] P.D. Negraes, B.Q. Jordao, V.E.P. Vicentini, M.S. Mantovani, Anticlastogenicity of chlorophyllin in the different cell cycle phases in cultured mammalian cells, Mutat. Res. 557 (2) (2004) 177–182, https://doi.org/10.1016/j.mrgentox.2003.10.012.

[73] J. Liu, F.B. Li, C. Liu, H.Y. Wang, B.R. Ren, K. Yang, E.L. Zhang, Effect of Cu content on the antibacterial activity of titanium-copper sintered alloys, Mater. Sci. Eng. C-Mater. Biol. Appl. 35 (2014) 392–400, https://doi.org/10.1016/j.msec.2013.11.028.

[74] L.Y. Cui, G.B. Wei, Z.Z. Han, R.C. Zeng, L. Wang, Y.H. Zou, S.Q. Li, D.K. Xu, S. K. Guan, In vitro corrosion resistance and antibacterial performance of novel tin dioxide-doped calcium phosphate coating on degradable Mg-1Li-1Ca alloy, J. Mater. Sci. Technol. 35 (3) (2019) 254–265, https://doi.org/10.1016/j.jmst.2018.09.052.

[75] E. Ringe, Shapes, plasmonic properties, and reactivity of magnesium nanoparticles, J. Phys. Chem. C 124 (29) (2020) 15665–15679, https://doi.org/10.1021/acs.jpcc.0c03871.

[76] C.X. Yang, G.Y. Yuan, J. Zhang, Z. Tang, X.L. Zhang, K.R. Dai, Effects of magnesium alloys extracts on adult human bone marrow-derived stromal cell viability and osteogenic differentiation, Biomed. Mater. 5 (4) (2010), https://doi.org/10.1088/1748-6041/5/4/045005.

[77] Z. Zhu, Q. Gao, Z. Long, Q. Huo, Y. Ge, N. Vianney, N.A. Daliko, Y. Meng, J. Qu, H. Chen, B. Wang, Polydopamine/poly(sulfobetaine methacrylate) Co-deposition coatings triggered by CuSO4/H2O2 on implants for improved surface hemocompatibility and antibacterial activity, Bioact. Mater. 6 (8) (2021) 2546–2556, https://doi.org/10.1016/j.bioactmat.2021.01.025.

[78] A. Perdikaki, A. Galeou, G. Pilatos, I. Karatasios, N.K. Kanellopoulos, A. Prombona, G.N. Karanikolos, Ag and Cu monometallic and Ag/Cu bimetallic nanoparticle-graphene composites with enhanced antibacterial performance, ACS Appl. Mater. Interfaces 8 (41) (2016) 27498–27510, https://doi.org/10.1021/acsami.6b08403.

[79] Y.Y. Zhong, T.T. Wang, Z.T. Lao, M.L. Lu, S. Liang, X.P. Cui, Q.L. Li, S.Q. Zhao, Au-Au/IrO2@Cu(PABA) reactor with tandem enzyme-mimicking catalytic activity for organic dye degradation and antibacterial application, ACS Appl. Mater. Interfaces 13 (18) (2021) 21680–21692, https://doi.org/10.1021/acsami.1c00126.

[80] Y. Zhang, S. Fu, L. Yang, G. Qin, E. Zhang, A nano-structured TiO2/CuO/Cu2O coating on Ti-Cu alloy with dual function of antibacterial ability and osteogenic activity, J. Mater. Sci. Technol. 97 (2022) 201–212, https://doi.org/10.1016/j.jmst.2021.04.056.

[81] S. Shao, V. Rajendiran, J.F. Lovell, Metalloporphyrin nanoparticles: coordinating diverse theranostic functions, Coord. Chem. Rev. 379 (2019) 99–120, https://doi.org/10.1016/j.ccr.2017.09.002.

[82] D. Mondal, S. Bera, Porphyrins and phthalocyanines: promising molecules for light-triggered antibacterial nanoparticles, Adv. Nat. Sci. Nanosci. Nanotechnol. 5 (3) (2014), 033002, https://doi.org/10.1088/2043-6262/5/3/033002.

[83] J.Y. Kou, D. Dou, L.M. Yang, Porphyrin photosensitizers in photodynamic therapy and its applications, Oncotarget 8 (46) (2017) 81591–81603, https://doi.org/10.18632/oncotarget.20189.

[84] E.S. Nyman, P.H. Hynninen, Research advances in the use of tetrapyrrolic photosensitizers for photodynamic therapy, J. Photochem. Photobiol. B Biol. 73 (1–2) (2004) 1–28, https://doi.org/10.1016/j.jphotobiol.2003.10.002.

[85] S. Singh, A. Aggarwal, N. Bhupathiraju, G. Arianna, K. Tiwari, C.M. Drain, Glycosylated porphyrins, phthalocyanines, and other porphyrinoids for diagnostics and therapeutics, Chem. Rev. 115 (18) (2015) 10261–10306, https://doi.org/10.1021/acs.chemrev.5b00244.

[86] I. Stojiljkovic, B.D. Evavold, V. Kumar, Antimicrobial properties of porphyrins, Expet Opin. Invest. Drugs 10 (2) (2001) 309–320, https://doi.org/10.1517/13543784.10.2.309.

[87] A. Almeida, A. Cunha, M.A.F. Faustino, A.C. Tomé, M.G.P.M.S. Neves, Chapter 5. Porphyrins as antimicrobial photosensitizing agents, in: Photodynamic Inactivation of Microbial Pathogens: Medical and Environmental Applications, 2011, pp. 83–160, https://doi.org/10.1039/9781849733083.

[88] T.L. Poulos, Heme enzyme structure and function, Chem. Rev. 114 (7) (2014) 3919–3962, https://doi.org/10.1021/cr400415k.

[89] M. Hüttemann, P. Pecina, M. Rainbolt, T.H. Sanderson, V.E. Kagan, L. Samavati, J. W. Doan, I. Lee, The multiple functions of cytochrome c and their regulation in life and death decisions of the mammalian cell: from respiration to apoptosis, Mitochondrion 11 (3) (2011) 369–381, https://doi.org/10.1016/j.mito.2011.01.010.

[90] K.D. Borah, J. Bhuyan, Magnesium porphyrins with relevance to chlorophylls, Dalton Trans. 46 (20) (2017) 6497–6509, https://doi.org/10.1039/C7DT00823F.

[91] E. Zhang, X. Wang, M. Chen, B. Hou, Effect of the existing form of Cu element on the mechanical properties, bio-corrosion and antibacterial properties of Ti-Cu alloys for biomedical application, Mater. Sci. Eng. C-Mater. Biol. Appl. 69 (2016) 1210–1221, https://doi.org/10.1016/j.msec.2016.08.033.

[92] Z. Lin, X. Sun, H. Yang, The role of antibacterial metallic elements in simultaneously improving the corrosion resistance and antibacterial activity of magnesium alloys, Mater. Des. 198 (2021), https://doi.org/10.1016/j.matdes.2020.109350.

[93] A.A. Buglak, M.A. Filatov, M.A. Hussain, M. Sugimoto, Singlet oxygen generation by porphyrins and metalloporphyrins revisited: a quantitative structure-property relationship (QSPR) study, J. Photochem. Photobiol., A 403 (2020), https://doi.org/10.1016/j.jphotochem.2020.112833.

[94] L. Sobotta, P. Skupin-Mrugalska, J. Piskorz, J. Mielcarek, Porphyrinoid photosensitizers mediated photodynamic inactivation against bacteria, Eur. J. Med. Chem. 175 (2019) 72–106, https://doi.org/10.1016/j.ejmech.2019.04.057.

[95] I.O. Bacellar, T.M. Tsubone, C. Pavani, M.S. Baptista, Photodynamic efficiency: from molecular photochemistry to cell death, Int. J. Mol. Sci. 16 (9) (2015) 20523–20559, https://doi.org/10.3390/ijms160920523.

[96] R.W.Y. Habash, R. Bansal, D. Krewski, H.T. Alhafid, Thermal therapy, part 1: an introduction to thermal therapy, Crit. Rev. Biomed. Eng. 34 (6) (2006) 459–489, https://doi.org/10.1615/CritRevBiomedEng.v34.i6.20.